JCI The Journal of Clinical Investigation

Vinculin influences essential processes in enteric nervous system development and Hirschsprung disease pathogenesis

Lifang Liu, Xixin Wang, Mingxuan Liang, Peiting Li, Cindy Yifei Yan, Patrick Ho-Yu Chung, Kenneth Kak-Yuen Wong, Asif Javed, Maria-Mercedes Garcia-Barcelo, Elly Sau-Wai Ngan

J Clin Invest. 2025. https://doi.org/10.1172/JCI198531.

Research In-Press Preview Gastroenterology Genetics

Graphical abstract

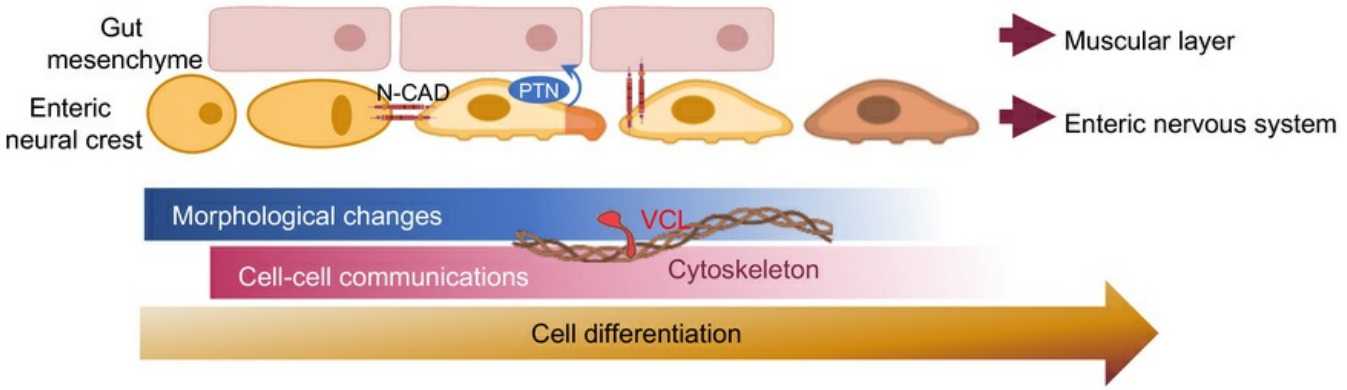

Vinculin influences essential processes in enteric nervous system development and Hirschsprung disease pathogenesis.

Lifang LIU[1], Xixin WANG[1], Mingxuan LIANG[2], Peiting LI[1], Cindy Yifei YAN[1], Patrick Ho-Yu CHUNG[1], Kenneth Kak-Yuen WONG[1], Asif JAVED[2,3], Maria-Mercedes GARCIA-BARCELO[1], Elly Sau-Wai NGAN[1*]

[1]Department of Surgery, [2]School of Biomedical Science, Li Ka Shing Faculty of Medicine, The University of Hong Kong, Pokfulam, Hong Kong.
[3]Translational Research Unit, Chulabhorn Research Institute, Bangkok, Thailand

*Corresponding authors:
Prof. Elly SW Ngan
Professor
Department of Surgery, School of Clinical Medicine
The University of Hong Kong,
Faculty of Medicine Building,
21 Sassoon Road, Pokfulam, Hong Kong, SAR, China.
Tel: 852-2831-5410
Email: engan@hku.hk

Competing Interests Statement
The authors declare no conflicts of interest

Abstract

Vinculin (VCL), a linker between cells and their environment, has rarely been linked to disease. This study examines the role of VCL in the development of the enteric nervous system (ENS) and its relationship to Hirschsprung disease (HSCR). Using whole-genome sequencing and in vitro assays, we identified four *VCL* mutations associated with HSCR, most causing loss of function. Neural crest-specific *Vcl* knock-out mice (*Vcl* cKO) displayed ENS defects resembling short-segment HSCR, including partial colonic aganglionosis and abnormal gut musculature. Single-cell transcriptomics revealed dysregulation of genes involved in neuronal differentiation and MAPK signaling. Spatial RNA sequencing revealed reduced ENS-mesenchyme interactions in *Vcl* cKO mice, accompanied by significant disruption of the Pleiotrophin (PTN) pathway; *Ptn* knock-out mice exhibited phenotypes similar to those of *Vcl* cKO mice, underscoring the importance of ENS-mesenchyme crosstalk. VCL works as a hub gene crucial for cell connection and signaling pathways essential for ENS formation. *VCL* deficiency subtly impacts various developmental stages and neighboring cells, cumulatively leading to a phenotype similar to short-segment HSCR. This research highlights the role of VCL in maintaining cellular interactions and signaling pathways, such as MAPK and PTN, which are crucial for ENS development and may inform therapeutic targets for ENS disorders.

Introduction:

Hirschsprung disease (HSCR) is the most common neurocristopathy, affecting approximately 1 to 1.3 out of every 5,000 newborns(1). This complex congenital disorder impacts the colon, resulting in the absence of nerve cells along a variable length of the colon due to incomplete colonization by enteric neural crest cells (ENCCs), which ultimately leads to functional intestinal blockage. Patients with a short aganglionic segment (S-HSCR), which includes the distal rectum and extends up to the rectosigmoid region, represent the most common form of HSCR, making up approximately 80% of cases. Long segment (L-HSCR) and total colonic aganglionosis (TCA) are the more severe forms, representing the remaining 20% of the cases.

Neural crest cells (NCCs) derived from the vagal region of the neural tube constitute the primary population of progenitor cells for the enteric nervous system (ENS) and begin to enter the esophagus around embryonic day 9.5 to 10.5 in mice. These cells proliferate extensively, migrate distally over long distances to colonize the developing gut, and differentiate into millions of neurons and glia, which are organized into a network to control bowel functions(2). A precise coordination of cell differentiation, migration, and ganglionogenesis is essential for the proper formation of a functional ENS(3).

Cell-to-cell communication signals among various cell populations are crucial for the development of the ENS. However, there remains limited knowledge about the specific molecules and signals involved in the interactions between different ENS cells and their neighboring cells that guide ENS development. To date, only a few homophilic adhesion molecules, such as N-cadherin, NCAM, and the L1 cell adhesion molecule (L1CAM), have been linked to ENCC migration. The loss of either N-cadherin or L1CAM leads to delayed ENCC migration and malformation of enteric aganglionosis(4). Moreover, the posttranslational modification of NCAM with polysialic acid (psNCAM) affects the

aggregation and migration efficiency of ENCCs(5, 6), but neither factor alone is sufficient to cause aganglionosis.

Vinculin (VCL) was identified as a crucial component of focal adhesions (FAs) and adherents junctions (AJs), playing a key role in mediating cell-matrix and cell-cell adhesions, respectively(7). It exists in two isoforms: the shorter VCL isoform, which is widely expressed, and the longer, muscle-specific metavinculin (meta-VCL). VCL interacts with over 14 putative binding partners at FAs, including talin, actin, and paxillin, to facilitate various cellular functions(8, 9). These interactions are essential for positioning VCL at the integrin signaling level, where it can respond to external stimuli(10). Moreover, these interactions are regulated by an auto-inhibitory mechanism involving intramolecular interactions between the head and tail domains of VCL(11, 12). The release of this auto-inhibition is necessary for the simultaneous binding of multiple ligands(13). On the other hand, VCL mediates cell-cell adhesion through a multistep process involving α-catenin, β-catenin, and YAP1(7, 14). *VCL* null mutants exhibit embryonic lethality by day 10 due to failures in rostral neural tube closure, abnormalities in forelimb development, heart malformations with reduced size and fewer myocytes than normal(15), and compromised development of cranial and spinal nerves(16).

A potential causal link between VCL and HSCR was first illustrated in our previous study, in which a mutation (M209L) in the *VCL* gene was identified in a syndromic patient presenting with HSCR disease and congenital cardiac defects, including ventricular septal defects (VSD) and valvular abnormalities (17). Subsequent functional analyses utilizing an induced pluripotent stem cell (iPSC)-based model demonstrated that the M209L substitution disrupts focal adhesion (FA) assembly, resulting in impaired migration and deficient neuronal/smooth muscle lineage differentiation of patient-specific iPSC-derived neural crest cells (NCCs). Correcting the *VCL* mutation effectively rescued the FA phenotype, leading to the restoration of NCC functions(17). At the molecular level, the M209L substitution disrupted the VCL-ACTIN

interaction, likely interfering with the morphological changes of the cells associated with various developmental processes(17). However, it remains largely unclear whether the ablation of *VCL* alone is sufficient to cause disease and its potential implications for the pathogenesis of HSCR.

In this study, we first re-analyzed the exome regions of the genome using our in-house whole-genome sequencing dataset of S-HSCR(18, 19) to explore the relevance of *VCL* in the pathogenesis of HSCR. Subsequently, we generated a mouse model with NCC-specific ablation of *VCL* to directly demonstrate its implications in ENS development. High-resolution and spatial RNA sequencing data further elucidated the molecular mechanisms involved and the sequential effects resulting from the loss of cell-cell and cell-matrix interactions. This highlighted the significance of interactions among ENS cells and their surrounding environment in both ENS formation and HSCR pathogenesis. Intriguingly, VCL does not operate through a single, dominating effect via a specific signaling pathway, as is often the case in Mendelian diseases. Instead, it functions as a hub gene, integrating various cellular processes during development, which can subsequently lead to disease when disrupted.

Result:

Multiple loss-of-function mutations in VCL were found in both syndromic and isolated HSCR patients.

To elucidate the role of *VCL* in the pathogenesis of Hirschsprung disease (HSCR), we re-analyzed a whole-genome sequencing dataset comprising 94 S-HSCR patients with comprehensive clinical records, which included thirteen patients presenting with both HSCR and VSD, representing approximately 13% of the cohort(19). In total, we identified seven *de novo* heterozygous mutations distributed across various exons of the *VCL* gene in nine HSCR patients (Supplementary Data 1 and Figure 1A). Among these, A977P mutation is located

within the functional domain of the muscle-specific isoform (isoform 1), which is not expressed in NCCs (Supplementary Figure 1), it is plausible that this mutation does not contribute to NCC-associated defects.

We then evaluated the potential impacts of the remaining six *VCL* mutations on focal adhesion (FA) assembly by measuring FA sizes, as described in previous studies(17). In brief, expression constructs carrying either wild-type (WT) or mutant *VCL* were overexpressed in the human cervical cancer cell line HeLa, and FAs were detected using immunocytochemistry with the FA marker Paxillin. The sizes of the FAs were measured and compared. Notably, four out of six mutations were found to be deleterious, leading to a reduction in FAs size, primarily located within the head or tail domains of VCL (Figure 1, B and C, and Table 1). The M209L substitution was identified in three non-consanguineous syndromic HSCR patients presenting with VSD and exhibited a prominent effect on FA assembly. Therefore, we further investigated the mechanism by which the M209L substitution disrupts FA assembly. Specifically, this mutation is situated in head domain 1 (Vh1) of VCL, and it may promote auto-inhibitory head-to-tail interactions. To test this hypothesis, we generated expression constructs incorporating either the head (amino acids 1-258) or tail (amino acids 879-1066) regions of VCL, tagged with FLAG or c-MYC, respectively. Both WT and M209L mutant head constructs, along with the c-MYC tagged tail construct, were co-expressed in HeLa cells, followed by co-immunoprecipitation assays. Our findings revealed that the M209L substitution enhances the head-to-tail interaction, likely resulting in VCL inactivation (Figure 1D). Moreover, VCL mutants exhibited a diminished binding affinity to phosphor-Paxillin (Figure 1E), which may account for the observed FAs defects. Importantly, impaired FAs assembly may reduce the ability of cells to respond to external stimuli and interact with their environment, thereby disrupting various cellular processes.

Neural crest-specific ablation of VCL caused partial colonic aganglionosis

To directly investigate the roles of VCL in the development of ENCCs, both copies of the *Vcl* gene were specifically deleted from NCCs using the *Wnt1-Cre* mouse line, resulting in *Vcl* conditional knock-out (cKO) mutants. These mutants exhibited both cardiac and enteric nervous system (ENS) defects and did not survive beyond a few hours after birth. In terms of ENS phenotypes, nearly all E18.5 mutants analyzed (n>20) showed varying degrees of colonic aganglionosis, as determined by acetylcholinesterase (AChE) staining. As demonstrated in Figure 2A, the ENS network did not fully cover the distal colon in the *Vcl* cKO mutants, whereas the ENS in the proximal and middle colon appeared unaffected and closely resembled that of the control group. We subsequently performed immunohistochemistry analyses on whole-mount colon preparations, consistently revealing aganglionic regions in the distal colon of the *Vcl* cKO mutants (Figure 2B). Interestingly, the neurons and glial cells adjacent to these aganglionic areas were not properly organized or distributed as ganglia, in contrast to the arrangement observed in the control (Figure 2C). We then quantified the number of HuD^+ neurons and $SOX10^+$ glial cells in the distal colon. In the control colon, both neurons and glial cells were evenly distributed with comparable density across 4-8 random views (600 mm^2 each) from 3 embryonic guts. The counts of neurons and glia were normalized against the total number of cells per view, as indicated by DAPI staining. In summary, the control group exhibited 41.84 ± 1.39% neurons and 22.65 ± 1.07% glia, resulting in a neuron-to-glia ratio of 1.89 ± 0.09. In contrast, in the comparable regions, the mutants displayed a lower percentage of neurons (34.56 ± 3.80%) and a higher percentage of glia (29.29 ± 3.07%), along with greater variability. The neuron-to-glia ratio in the mutants was significantly reduced to 1.20 ± 0.12 (Figure 2C).

We then generated *Vcl* cKO with a YFP background (*Wnt1-Cre; Rosa26*^{YFP}*;Vcl*$^{f/f}$), allowing for the labeling of ENCCs with YFP. Additional immunohistochemical analyses were performed on sections of the distal colon from E18.5 control and mutant specimens. Consistent

with the data obtained from whole-mount staining, we observed a significant reduction in the percentage of committed neurons ($PHOX2B^{+}SOX10^{-}YFP^{+}$), accompanied by an increase in the number of uncommitted ENCCs ($PHOX2B^{+}SOX10^{+}YFP^{+}$) (Figure 3A). In sum, *Vcl* mutants displayed partial aganglionosis and exhibited an immature ENS.

Upon analyzing the cross-sections of the mutant guts at E18.5, we observed that the smooth muscle in the *Vcl* cKO colon was less densely packed and less organized, with a notable reduction in the thickness of the mesenchymal layer (Figure 3B). Since *Vcl* was specifically deleted in NCCs, this is likely a secondary consequence of the ENS defect, suggesting that the ENS plays a crucial role in the development and patterning of the mesenchyme and smooth muscle.

Aberrant migration of ENCCs in Vcl mutants

We reasoned that the incomplete colonization of the distal colon in mutants would be the result of migration defects of ENCCs. Thus, we collected embryonic guts from E11.5 to E13.5, which is the key developmental window for gut colonization, and analyzed the migration of ENCCs in the ex vivo guts during these stages. A slight but significant delayed migration of ENCCs was observed in E11.5 *Vcl* cKO embryonic gut (Figure 4A).

To investigate their migration patterns, live imaging was conducted over a period of 12 to 15 hours using E12.5 hindguts to observe the behavior of YFP-labelled ENCCs in both control and mutant conditions. The control ENCCs exhibited a distinctive migration pattern, moving in chains that often converged and diverged as they elongated distally to invade the uncolonized regions of the gut. The nodes formed at the intersections of these ENCC chains, along with the interconnecting chains themselves, are proposed to play a role in guiding the arrangement of ganglia into a lattice-like neuronal network(20). ENCCs in the control gut remained interconnected as continuous strands throughout their migration (Figure 4B). In

contrast, the migration of ENCCs was disrupted in *Vcl* cKO mutants. Although these mutant cells could migrate towards the distal end of the hindgut, they displayed an inconsistent migration trajectory. More significantly, the mutant cells failed to establish a migratory chain at the migratory front, resulting in a number of solitary ENCCs (Figure 4B and Supplementary Video 1). We then further monitored the behavior of ENCCs at the migratory front. While the migration direction of ENCCs in both *Vcl* cKO and control groups was similar, with a tendency to move toward the distal end of the hindgut, the mutant ENCCs consistently deviated from the primary migratory path (Supplementary Figure 2A). Additional analysis of their migration tracks revealed that the average speed of cell migration was somewhat reduced in the mutants (Supplementary Figure 2B), whereas their persistence (defined as the ratio of net distance traveled to total distance traveled) remained comparable to that of control cells (Supplementary Figure 2C). Alongside the irregular migratory patterns observed in VCL-deficient ENCCs, the overall net migration speed was also diminished (Figure 4B). By E13.5, a distinct neuronal meshwork had formed in the control gut; however, the mutant ENCCs were unable to maintain connections with neighboring cells, leading to a significant presence of solitary ENCCs at the distal end of the hindgut (Figure 4C). This observation indicates that the connections between ENCCs were disrupted during migration, which likely interferes with subsequent ganglionogenesis.

Reconstruction of the differentiation paths of ENCCs reveals that loss of VCL delays their differentiation along the Branch A

In addition to the migration defect, the mutant exhibited a reduced number of mature neurons and an increased presence of uncommitted ENCCs, as illustrated in Figure 2C and Figure 3A. This suggests a potential differentiation defect in the mutant ENCCs. Notably, delayed differentiation was observed as early as E13.5, with the differentiation defect

becoming more pronounced by E15.5 (Supplementary Figure 3). Therefore, we analyzed the transcriptomes of ENCCs that were isolated and enriched through fluorescence-activated cell sorting (FACS) from 7 guts of control (*Wnt1-Cre; Rosa26*^{YFP}) and *Vcl mutant* (*Wnt1-Cre; Rosa26*^{YFP}*;Vcl*$^{f/f}$) embryos at E13.5 and E15.5 (Supplementary Figure 4), each from 2-3 litters. This was performed using single-cell RNA sequencing (RNA-seq) with 10X Genomics to explore further how the loss of *Vcl* influences the molecular dynamics of ENCCs along their differentiation trajectories. Additionally, we carried out 10X Visium spatial transcriptomics (ST) analysis on sagittal sections of E13.5 embryos to investigate how alterations in signaling among various ENS cells and their neighboring cells contribute to the observed defects in the mutants. By cross-referencing our scRNA-seq and ST-RNA-seq datasets, we aimed to clarify the molecular mechanisms by which VCL governs ENCC development and their interactions with adjacent cells. Human induced pluripotent stem cell (hiPSC)-based and mouse models were then used for functional validation. A schematic summarizing our analysis pipeline is presented in Figure 5A.

After performing quality control on the scRNA-seq data, we identified a total of 30,157 cells, with each cell exhibiting an average of 3,677 genes and 13,860 unique molecular identifiers (UMIs) detected (refer to Supplementary Figure 5 and Supplementary Data 2). To refine the differentiation trajectories, we integrated our dataset with a previously published dataset of E18.5 ENS cells and reannotated them based on the expression of canonical marker genes and lineage-specific transcriptional factors identified in the original study (Supplementary Figure 6). The Uniform Manifold Approximation and Projection (UMAP) plots revealed five cell clusters comprising three distinct differentiation branches: neuronal, which includes inhibitory (Branch A) and excitatory (Branch B) neurons, and glial lineages (Figure 5B). All paths originated from the highly proliferative bipotent progenitors (BP) characterized by high expression of *Mki67*, *Ube2c*, *Cdc20*, and *Ccnb1*. The cells on the

neuronal differentiation trajectory progressed through a neuronal intermediate stage, Neuroblast, which is marked by early neuronal markers (*Tubb3*^{high}/*Elavl4*^{high}/*Cartpt*$^{-}$/*Prph*$^{-}$), before diversifying into two branches distinguished by the complementary expression of *Etv1* and *Bnc2*, representing Branch A and Branch B neurons, respectively. By E15.5, Branch A constituted the predominant neuronal population, co-expressing markers of inhibitory neurons like *Nos1* and *Vip*, while a smaller subset expressed *Bnc2* with a reduction in *Etv1* expression, corresponding to Branch B excitatory neurons. In terms of the glial lineage differentiation trajectory, glial progenitors (GPs) displaying high levels of *Sox10* and *Fabp7* began to emerge at this stage. Additionally, a distinct population of progenitors that expressed unique marker sets referring to the enteric mesothelial fibroblasts (ENMFBs) was identified (Figure 5, B and C, Supplementary Data 3).

We subsequently examined the impact of *Vcl* loss on cell composition. Both the control and mutant groups contained all five clusters of neural cells and the ENMFB cluster. Interestingly, the *Vcl* mutant showed an increased proportion of BP cells at E13.5, coupled with a decrease in Branch A neurons at both E13.5 and E15.5 (Figure 5D). Further RNA velocity analyses revealed that the differentiation trajectories in both control and *Vcl* mutant populations were similar (Figure 5E), indicating that the absence of *Vcl* does not disrupt the differentiation of ENCCs toward a specific lineage, nor does it introduce a differentiation bias that would lead to a reduction in Branch A.

To investigate the heterogeneity of cells within the BP-to-Branch A lineage, we aimed to order the cells in pseudotime and infer the trajectories along this differentiation path. We began by performing a Principal Component Analysis (PCA) to reorganize all the cells in the BP-to-Branch A lineage. The distribution of cells projected to principal components 1 (PC1) and 3 (PC3) illustrated a continuous pseudotemporal trajectory from the BP to Branch A. Consequently, we inferred the pseudotime based on these two dimensions (Supplementary

Figure 7, A-C). As shown in Figure 5F, both control and mutant cells from E13.5 and E15.5 exhibited a well-ordered arrangement along the pseudotime of differentiation. In the *Vcl* mutant, the BP cells at E13.5, Neuroblasts at E15.5, and Branch A neurons demonstrated significantly lower pseudotime values compared to the control cells, indicating a delayed differentiation along the Branch A neuronal lineage and immaturity of the Branch A neurons (Figure 5F and Supplementary Figure 7D). Consistently, a significant reduction in the expression of Branch A marker genes, coupled with elevated expression of the proliferative marker *Mki67*, was observed, suggesting fewer mature Branch A neurons in *Vcl* mutant (Figure 5G).

In accordance with the RNA-seq data, a significantly greater number of ENCCs remained proliferative ($Ki67^+$) in the mutants at E18.5, while only post-mitotic ENCC derivatives were observed in the control group at this stage (Figure 6A). This finding further suggests the immature nature of the ENS in the mutants. Consistent with this observation, there were significantly fewer mature neurons (HuD^+) and a larger population of immature neurons (HuD^+SOX10^+) in the mutants compared to the controls (Figure 6B). Notably, the inhibitory lineage ($nNOS^+$) appeared to be the most severely impacted (Figure 6C), which corresponds to neurons in Branch A.

The overarching roles of VCL in the neuronal lineage differentiation of ENCCs

We aimed to elucidate the mechanisms responsible for the delayed neuronal differentiation and maturation. To that end, we conducted further analyses on the four most impacted cell states: BP at E13.5, Neuroblast at E15.5, and Branch A neurons at both E13.5 and E15.5 (Figure 7A). We identified a total of 3,016 differentially expressed genes (DEGs) (*FDR*<0.01), which included 35 and 14 consistently downregulated and upregulated along the BP-to-Branch A trajectory, while 2,967 genes showed a dynamic expression profile. To identify the most biologically relevant DEGs, we employed a two-tier approach that considered

both changes in expression levels and the biological roles of the genes. First, we conducted Gene Ontology (GO) enrichment analysis on the DEGs across each cell state, categorizing them according to biological processes. We then focused on the top 50 GO pathways in each cell state and calculated the corresponding pathway scores for both control and mutant samples (Supplementary Data 4). The ten most significantly disrupted biological processes within each cell state, comprising 640 DEGs, were selected for further examination based on changes in pathway scores. Subsequently, we examined how these 640 DEGs could influence cellular progression by re-clustering them alongside their potential driving genes, specifically transcription factors (TFs), utilizing a gene regulatory network (GRN) inference strategy (Figure 7B and Supplementary Data 5). Among the 640 DEGs, 447 were identified as potential target genes of *E2f1*, *Egr1*, and *Klf7* based on expression correlation and motif binding analyses. These target genes were utilized to construct a GRN, which was organized into four distinct modules based on their regulatory relationships. We also re-correlated the genes within these modules with their respective cell states by analyzing the dynamic expression profiles of three hub transcription factors: *E2f1*, *Egr1*, and *Klf7*, in control and *Vcl* mutant cells along the differentiation trajectory (Supplementary Figure 8). Notably, *E2f1* exhibited significant differential expression primarily in the BP, while *Klf7* showed disruption specifically in the Branch A neurons. In contrast, expression of *Egr1* decreased consistently across the entire trajectory from BP to Branch A in mutant cells, with the greatest difference from the control cells in Neuroblast (Supplementary Figure 8, A and B). Similar dynamic regulons were also observed consistently (Supplementary Figure 8C). Consequently, we designated Module 1 to BP, Module 2 to Neuroblast, and Modules 3 and 4 to the Branch A neurons (Figure 7C). To assess the impact of *Vcl* loss on these module genes, we then calculated the module scores for both control and mutant cells. The results indicated that all modules exhibited significantly diminished signals in their corresponding cell states in *Vcl* mutants (Figure 7C), suggesting

that the absence of *Vcl* disrupts the cellular processes governed by these module genes.

In line with these observations, genes within modules showed stronger expression correlation with *Vcl* compared to other genes (Supplementary Figure 8D). Moreover, VCL demonstrated protein-protein interactions and co-expression relationships with numerous genes across all four modules (Figure 7, B and D). These results suggested that VCL mediates the genes in these modules directly or indirectly to govern various cellular processes along BP-to-Branch A differentiation. For instance, integrin beta1 (*Itgb1*) within Module 2 is essential for ENCC migration and subsequent ganglionogenesis(20-22). Another gene, transgelin 2 (*Tagln2*), encoding an actin-binding protein that is linked to the migration and proliferation of tumor cells(23), also interacts directly with VCL at the protein level, which may suggest that the cell migration process is affected in *Vcl* mutants. In Module 3, VCL interacts with catenin alpha-2 (CTTNA*),* which links cadherin adhesion receptors and the cytoskeleton to regulate cell-cell adhesion and differentiation in the nervous system(24). In addition, Alpha actinin-1 (ACTN1) is a cross-linking protein that interacts with F-actin, playing a crucial role in anchoring actin to various intracellular structures. Morphological changes are essential for initiating neuronal differentiation; thus, VCL likely interacts with these proteins, governing the morphological changes necessary to support subsequent neuronal differentiation.

Additionally, the GO enrichment analysis of the genes within the modules highlighted several disrupted biological processes. Notable findings include neurogenesis within BP (Module 1), cell junction assembly in both BP and Neuroblast modules (Modules 1 and 2), morphology-related regulation and actin filament organization affecting both neuroblasts and Branch A neurons (Modules 2 and 3), and synaptic vesicle function specifically within Branch A neurons (Module 4) (Figure 7E). According to the Kyoto Encyclopedia of Genes and Genomes (KEGG) database, the up-regulated genes were associated with neuronal disorders while the significantly down-regulated genes were involved in MAPK and Rap1 signaling

pathways, which are critical for neuronal differentiation (25) (Figure 7F and Supplementary Data 6). In summary, the results indicate that *VCL* deficiency disrupts multiple cellular processes involved in neuronal lineage differentiation. This disruption begins at the early stages, affecting cell morphogenesis and cell-cell adhesion, which in turn impacts the BP and Neuroblast stages. Additionally, the maturation of Branch A neurons is notably hindered, with the MAPK and RAP1 signaling pathways being the most significantly affected. Ultimately, these changes contribute to a delay in the formation of mature Branch A neurons.

To evaluate the direct involvement of VCL in the neuronal lineage differentiation of ENCCs, we established an in vitro model using human induced pluripotent stem cells (hiPSCs). First, an inducible CRISPR/Cas9 (iCas9)-hiPSC line was used to specifically knock down *VCL* in ENCCs or committed neuronal progenitors (NPs), where the expression of Cas9 protein was induced by the addition of doxycycline (DOX) (Figure 8A). A two-step differentiation protocol was used to model ENCC-to-neuron differentiation. iCas9-hiPSCs were first directed to the NCC lineage by dual-SMAD inhibitors (LDN193189 and SB431542) with a WNT agonist (CHIR99021) and then caudalized with retinoic acid (RA) to obtain posterior/vagal NCCs (hereafter referred to as hENCCs), which were further enriched using FACS and characterized based on the expression of the NC-specific surface markers (HNK1, $p75^{NTR}$, CD49 and SOX10) (Supplementary Figure 9) as described previously(17, 26). The neuronal lineage differentiation of hENCCs was then induced by culturing the hENCCs in neuronal differentiation medium supplemented with various neurotrophic factors (see Supplementary Methods). The *VCL* gene was knocked down in hENCCs or committed NPs by transfecting cells with *VCL*-targeting gRNAs and in the presence of doxycycline on Day 12 or Day 15, respectively (Figure 8A). By day 30 of differentiation, the neuronal differentiation capacity of the cells was monitored based on the expression of neuronal markers (neurofilament, NF and Protein gene product 9.5, PGP9.5). When *VCL* was knocked down (KD) at NCC stage on Day 12, the mutant cells

showed a weaker ability to aggregate together, and this severely abolished the subsequent neuronal lineage differentiation. As a result, significantly fewer cells were obtained at day 30 of differentiation in *VCL* KD group, and among them, a lower percentage of cells expressing neuronal markers (NF^+ or $PGP9.5^+$, a marker for clinical diagnosis) compared to the control group (Figure 8B and Supplementary Figure 10A). Similarly, even if we bypassed the neuronal initiation step and KD *VCL* on day 3 after culturing ENCCs in neuronal differentiation medium, the percentage of neurons was significantly lower in the KD group, while the total number of cells was more comparable (Figure 8C and Supplementary Figure 10B). Our scRNA-seq analysis revealed the MAPK pathway as the most significantly disrupted signaling pathway in VCL-deficient cells, particularly in Neuroblast and Branch A neurons. This disruption of the pathway was consistently observed in hENCCs-derived neurons when *VCL* was knocked down (Figure 8D). These findings suggest that VCL is essential for the activation of the MAPK pathway, which is crucial for initiating neuronal lineage differentiation of ENCCs and their subsequent maturation.

Spatial transcriptomic analysis reveals disruption of cell-cell interactions among ENCCs and with the gut mesenchyme in Vcl cKO

VCL is essential for cell-cell interactions and our scRNA-seq data showed perturbation of integrins and cell junction assembly in *Vcl* mutant ENCCs. Thus, we also examined whether loss of *Vcl* in ENCCs perturbs the communications between ENS cells and their neighborhoods, which may interrupt the ENS development. To this end, we conducted spatial-RNA-seq (ST-seq) analysis on sagittal sections of E13.5 embryos, utilizing replicate tissue sections spaced approximately 16 microns apart. The sequencing of these samples was performed to a median depth of 171,916,081 reads (with an interquartile range of 153,220,340 to 200,680,799), resulting in an average of 6,845 genes and 26,110 unique molecular identifiers (UMIs) per spot (Supplementary Figure 11A). The gut regions were manually delineated based

on histological images in each section. We then integrated and jointly analyzed the replicate sections from the control and mutant groups to cover more independent regions of the gastrointestinal tract. Subsequently, deconvolution was employed to estimate the cell type composition for each ST data spot, using a published scRNA-seq dataset of embryonic guts at the same developmental stage as a reference. Through this analysis, ST spots were categorized into specific gut regions according to the relative expression of genes characteristic of the large intestine (*Fxyd4, Muc2, Ntm, Fabp1, Cdx2, Satb2*), small intestine (*Tff3, Tdo2, Lum, Gpr50, Agr2, Sulf1*), and stomach (*Barx1, Sox2, Gata4, Igf1, Nkx2-5*) (Supplementary Figure 11, B and C). Using a similar approach, the spots were further annotated as epithelial (EPI), mesenchymal (MES), and neural crest (NC) cells. Only cells that expressed *YFP* (*YFP*$^{+}$) within these regions were classified as NC (Supplementary Figure 11, D and E).

Among the four sections, we focused on Control 1 and Mutant 2, which had more comparable numbers of various cell types and covered a larger region of the large intestine compared to the other two sections. In particular, the ENS phenotypes of *Vcl* cKO were only observed in the distal colon, so the subsequent analyses were restricted to those regions identified as the large intestine in these two sections at similar spatial locations (Figure 9A). Within the selected regions, comparable interactions among EPI and MES were found in the control and mutant (Supplementary Figure 12, A and B), while no common communication between NC and MES was detected. It is likely attributed to the specific deletion of *Vcl* in NCCs, abolishing the communications between NC and their neighboring cells in the mutant. We therefore focused on the interactions within NC and other cell types (Supplementary Data 7). The overall interactions related to NCCs in the *Vcl* mutant exhibited a reduction in both quantity and interaction strength (Figure 9B). Among the 20 interrupted pathways detected, NCAM and PTN pathways exhibited the highest probability of contributing to the reduced interactions found in the mutant (Figure 9C and Supplementary Figure 12C). To further

analyze the disrupted cell-cell interactions, we categorized communications by cell-type pairs and identified the top three interactions ranked by probability in each cell-type pair (Figure 9D). Among the signal flows from NC to MES, two interactions related to PTN (*Ptn-Sdc2/3*) were significantly affected, which aligns with the observed reduction in PTN expression in ENCCs at E18.5 (Figure 10A). The interaction between *Fn1* and the *Itga5+Itgb1* pair was found to be the most impacted signal flow from MES to NC, exhibiting the highest probability. Additionally, a decrease in ITGB1 expression was detected in ENS cells at E18.5 (Figure 10B). Limited NC-NC interactions were detected from the ST data, likely due to the sparse number of NC spots available. Therefore, we investigated NC-NC interactions using scRNA-seq data from E13.5 (Supplementary Figure 13). Notably, we consistently observed reduced Cdh2-Cdh2 interactions in *Vcl* cKO mutants across both the scRNA-seq and ST-seq datasets, alongside diminished N-cadherin (CADH2 encoded by *Cdh2*) expression levels in NC cells (Figure 10, C and D). In summary, *Vcl* deficiency disrupts a crucial signaling pathway PTN (27, 28) and affects adhesion molecules (NCAM and CADH2) (20-22) that are vital for cell-cell interactions, cell migration, and subsequent gangliogenesis. The compromise of these signalings and adhesion molecules impairs cell-cell communication and interactions between NC and neighboring cells, ultimately hindering the development of the ENS.

Loss of Ptn perturbed the formation of circumferential smooth muscle cell layer in Vcl cKO and Ptn KO

Our spatial RNA sequencing data revealed multiple disruptions in cell-cell communication between ENCCs and MES cells in the *Vcl* cKO colon. While the functions of NCAM and CADH2 in the ENS are well-established, the role of PTN remains less defined. Our findings suggest that PTN is the most significantly affected pathway mediating communication between ENCCs and MES cells. Further expression analysis demonstrated that

PTN is expressed in both ENCCs and gut MES cells; notably, its expression in ENCCs increases with developmental stages, whereas in MES cells, the highest expression is found at E15.5 (Figure 11A and Supplementary Figure 14). Notably, both ENCCs and MES cells exhibited downregulation of PTN in *Vcl* cKO mutants across all developmental stages examined. We next sought to understand the biological functions of PTN signal in ENS and gut development. The $Ptn^{-/-}$ mutants consistently exhibited ENS defects resembling the *Vcl* cKO mutants, but with less severity. They included hypoganglionic colon (Figure 11B), a disorganized ENS network of reduced neuron-to-glia ratio (Figure 11, C and D) and immature ENS with reduced percentage of post-mitotic neurons (Figure 11E). Intriguingly, PTN is essential for the smooth muscle lineage differentiation of MES cells, which contribute to the formation of the two circumferential smooth muscle layers of the colon: the lamina muscularis interna and lamina muscularis externa. $Ptn^{-/-}$ mutants at E15.5 exhibited a thinner lamina muscularis interna and a delayed spatial separation between the two smooth muscle layers. A similar phenotype was observed in *Vcl* cKO mutants, where only a few Calponin (CNN1) - positive smooth muscle cells were present in the lamina muscularis externa at this stage (Figure 11F). This phenotype likely results from impaired smooth muscle differentiation.

Discussion

VCL is a critical molecular component involved in mediating cellular interactions with the extracellular environment. To date, only three *VCL* mutations have been reported. L954del and R975W were found to be associated with either sporadic or familial dilated cardiomyopathy. These two mutations specifically affect the tail region of the VCL protein, potentially disrupting the binding of VCL with actin and paxillin(29, 30). The M209L mutation, on the other hand, located in the head region of VCL protein, was later identified in a syndromic patient who presented with HSCR disease and congenital cardiac defects(17).

Through reanalysis of our in-house sequencing dataset combined with functional validation, we identified four loss-of-function mutations in the *VCL* gene in seven HSCR patients. Notably, the M209L mutation was identified in three patients with syndromic short-segment HSCR exhibiting both ENS and cardiac anomalies. This finding prompted further investigation into the role of VCL in neural crest development and its implications in neurocristopathies.

In mice, we found that NC-specific deletion of *Vcl* has a severe impact on the development of the NCCs. The mice exhibited cardiac outflow tract and ENS defects mirroring the syndromic HSCR patients. *Vcl* cKO ENS exhibited hypoganglionosis or partial aganglionosis in the distal colon. Structurally, the hypoganglionic region resembles the transition zone of the HSCR bowel, characterized by a mixture of abnormal ganglion cells and nerve structures. This area is also distinguished by a thicker muscularis externa layer and a comparatively thinner muscularis interna relative to the ganglionic region(31). In E18.5 embryos, mutant colons consistently exhibited a reduced quantity of meconium, indicative of potential dysmotility within the mutant gastrointestinal tract. *Vcl* cKO died a few hours after birth, precluding a more detailed analysis in the postnatal ENS.

The colonic hypoganglionosis of *Vcl* cKO was likely attributed to defects not only in cell-cell interactions but also in neuronal differentiation of ENCCs. Loss of cell-cell interaction caused only a slight delay in gut colonization, but in conjunction with immature neuronal differentiation, it significantly disrupted ganglion formation, thereby greatly perturbing the establishment of the ENS network in the bowel. As observed in short-segment HSCR patients, the distal colon of the mutant was the most affected, with many more immature or partially committed ENS neurons residing in the distal colon. It raises the possibility that these partially committed ENS neurons remain migratory and migrate along with the wavefront cells, reaching the distal colon. The lack of coordination between migration and differentiation, along with disrupted cell-cell interaction, interfered with ganglion formation, leading to colonic

hypoganglionosis.

VCL and integrins(10), as well as the roles of integrins in mediating gut colonization by ENCCs(32), are well-documented. However, the influence of VCL on the neuronal lineage differentiation of ENCCs remains unclear. To address this, we conducted single-cell transcriptomic analyses of ENS cells isolated from E13.5 and E15.5 embryonic guts, stages during which distinct differentiation trajectories are established. Unlike abolishing a specific signaling pathway associated with cardiac neural crest defects(33), VCL appears to have a more prominent role in regulating morphological changes that promote neuronal differentiation and support neuron maturation through interactions with the cytoskeleton. The dysregulation of the MAPK pathway was identified as a major factor contributing to differentiation defects beyond morphological abnormalities. This pathway acts as a central signaling cascade integrating multiple key signals involved in ENS development, including the GDNF and ERBB pathways. Although some disruptions were observed in certain ERBB pathway genes, these were limited to two subpopulations. Notably, most *VCL* carriers lack the *RET* variant, suggesting that *VCL* may be a RET-independent gene associated with HSCR; however, additional studies with larger patient groups are needed to confirm this hypothesis. VCL is implicated in various stages of neuronal lineage progression, spanning from BP to neuroblast to Branch A neurons. It influences critical processes, such as cell adhesion and cytoskeletal dynamics, which are essential for morphological modifications and axonogenesis, ultimately contributing to a delay in cell advancement along the developmental trajectory if lost. Consistent with *in vivo* observations, using the hiPSC-based model, inducible deletion of *VCL* before and after the start of differentiation also prevented the neuronal lineage from forming, highlighting the role of VCL in early stages of ENS development.

In addition to the cell-autonomous effect, the loss of VCL in ENCCs severely interfered with the interactions among ENS cells and their neighbouring (MES) cells, as revealed by

spatial transcriptomic analysis. Down-regulation of N-cadherin (CADH2) disrupts cell-cell interactions among ENCCs, which may explain the presence of solitary ENS cells at the migratory front of the mutant gut and retarded ganglion formation. Intriguingly, we identified PTN as a key regulator in the signaling pathway between ENCCs and gut mesenchymal cells. In the central nervous system, PTN modulates processes such as cell migration, neural progenitor proliferation and self-renewal, neurite outgrowth, and synaptic plasticity through its interaction with multiple receptors, including syndecan (SDC)(34), and the subsequent activation of critical signaling cascades such as c-SRC, PI3K, and ERK1/2(35). Although PTN has previously been regarded as a growth factor secreted by gut mesenchyme(36), its specific functions within the ENS have remained poorly understood. In this study, we revealed a role for PTN, demonstrating that it not only influences ENCC differentiation but also functions as an ENCC-secreted factor that mediates gut mesenchyme development, contributing to the formation of the two distinct muscle layers of the bowel. Based on our data, we found no significant correlation in expression between these *Vcl* and *Ptn* genes (Figure 7D). The reason for the downregulation of PTN in the MES of *Vcl* cKO remains unclear. Considering that elevated PTN expression occurs in mature enteric neurons and that its expression is influenced by various growth factors(37, 38), we speculate that the immature status of ENS neurons and MES may contribute to the reduced PTN expression observed. Alternatively, its changes could be the result of the loss of cell-cell interactions in *Vcl* cKO. Abnormal muscle layers in HSCR bowel suggest ENS might support muscle development(31), but little is known about the specific molecules and signals guiding these cellular interactions during gut development. Therefore, further research is necessary to elucidate the specific roles of PTN in the ENS and/muscle development, as well as to understand its regulatory mechanisms.

In summary, we identified VCL as a hub gene coordinating the interactions between ENS and MES that are essential for gut development. VCL modulates multiple signaling

pathways involved in ENS development, and it exerts a subtle and continuous influence across various stages of ENS formation. Despite notable differences between humans and mice, which may impact mutation penetrance, the mouse still represents the best in vivo model for studying disease mechanisms. Here, we showed that the accumulation of minor disruptions caused by the loss of VCL ultimately leads to a phenotype characterized by partial aganglionic or hypoganglionic bowel, similar to features seen in short-HSCR. These subtle changes in signaling pathways and cell processes may represent a common, overarching mechanism underlying the pathogenesis of short-HSCR.

Materials and Methods:

Sex as a biological variable

Our study examined male and female patients and mice, and similar findings were observed in both sexes.

Patients

We reanalyzed our in-house whole-genome and whole-exome sequencing datasets(18, 19, 39) to identify potential mutation(s) affecting *VCL*. A total of 94 sporadic (no family history) HSCR patients with short-segment aganglionosis were included in this study. An in-house program KGGSeq(40) was used to assess the variant pathogenicity, which made use of valuable biological resources and knowledge, providing a comprehensive and efficient framework to filter and prioritize genetic variants from whole-exome and whole-genome sequencing data.

Construct construction

The full-length, head, and tail domains of human *VCL* (NM 00373) were obtained by PCR with specific primers (Supplementary Table 1) and subcloned into pCMV-GFP (Addgene, Plasmid #11153), pFLAG-CMV2 expression vector (Sigma), and pCMV-Myc-N (Clonetech), respectively. HSCR-associated mutations were then introduced into VCL expression constructs using the QuikChange Lightning Site-Directed Mutagenesis Kit (Agilent Technologies) with specific primers listed in Supplementary Table 1 according to the manufacturer's protocol. The wild-type and mutated *VCL* expression constructs were subsequently transfected into HeLa cells and subjected to immunofluorescent and pull-down assays.

Mice

Wnt1-Cre (strain# 022137), *Rosa26*^{YFP} (strain# 006148) and *Vcl*$^{f/f}$ (strain# 028451) mice were purchased from Jackson Lab. *Ptn* heterozygous knocKOut (T028403) mice were purchased from GemPharmatech.

Generation of an inducible Cas9 human induced pluripotent stem cells (iCas9-hiPSCs)

To generate a hiPCS line with an inducible expression of Cas9, the inducible cassettes, one containing the iCas9 coding sequence(41) under the regulation of the tight TRE promoter and the other carrying the M2rtTA tetracycline response element(42), were sequentially targeted into the AAVS1 loci by CRISPR-Cas9D10a nickase-mediated homologous recombination with two gRNAs (Supplementary Table 1). It was followed by selection with puromycin and neomycin, and the properly targeted neomycin and puromycin-resistant clones were selected using PCR. The inducible expression of Cas9 was validated by Western blot.

Derivation of enteric neural crest (ENCC) and neuronal progenitors (NPs) from iCas9-iPSC lines

A dual SMAD-inhibition protocol was used to generate hENCCs from hiPSC. The hENCCs were enriched by FACS with antibodies against p75^{NTR} and HNK-1 at day 10 of the differentiation. The FACS-enriched hENCCs were then cultured in neuronal differentiation medium for 10 and 20 days to generate early and late NPs, as described(17, 26, 43). *VCL* was deleted either on ENCC or at day 4 of differentiation by the addition of 2 μg ml^{-1} doxycycline and followed by transfection of *VCL*-targeting gRNAs.

Co-IP & Western blotting

co-IP was performed as previously described(44). In brief, cell lysates were incubated with anti-GFP or anti-FLAG M2 Magnetic Beads (Sigma, M8823) overnight at 4 °C. Antibody/protein complexes were washed with lysis buffer for four times and analyzed by Western Blotting. For Western blotting, protein lysates were separated on 8-12% SDS-polyacrylamide gels and blotted onto nitrocellulose membranes. The membranes were then incubated with primary and secondary antibodies (Supplementary Table 3 & S4).

Acetylcholinesterase (AChE) stain

The Acetylcholinesterase Rapid Staining Kit (MBL) was used to stain the ENS following the manufacturer's protocol.

Immunofluorescence studies

Immunocytochemistry & live imaging

Cells, whole mounts and sections of embryonic guts were fixed in 4% PFA, incubated in blocking buffer followed by primary and secondary antibodies (Supplementary Table 3 and 4) and counterstained with DAPI. For whole-mount staining, a clearing step was included by incubating the samples in Murray's Clear solution as described previously(44). All immunofluorescence images were captured using Carl Zeiss LSM 800 or LSM900 confocal microscope.

Carl Zeiss LSM 800 was also used for live imaging where Z-stack images were captured every 5 minutes for 12-15 hours as described previously(45). Immunofluorescence images and live imaging were processed and analysed using ImageJ (NIH) and Chemotaxis and Migration Tool plugin (ibidi), respectively.

Droplet-based single-cell RNA-sequencing (scRNA-seq) and spatial RNA-seq

The FACS-sorted cells were then subjected to droplet-based scRNA-seq using Chromium Single Cell platform and Single Cell 3' Library Kits (10x Genomics). Spatial transcriptomics was carried out using the 10x Genomics Visium platform with Visium Spatial Gene Expression Slides & Reagent kits with four sagittal sections from control and mutant. Details of the bioinformatic analysis are included in the Supplementary methods.

Statistical analysis and data visualization

Individual data points per mouse (5-6 animals per genotype) and means ±SEM are displayed in the figures. Data were analyzed using an unpaired 2-tailed Student's *t* test or one-way ANOVA. $P<0.05$ was considered significantly different (*: $P<0.05$; ***: $P<0.001$). Statistical analyses and data visualization were performed using Prism 10. In scRNA-seq data analysis, Empirical Bayes moderated T-test implemented in Scanpro was used for the cell type proportion comparison, with Benjamini-Hochberg-adjusted *P* value<0.05 considered significant. Two-sided unpaired Wilcoxon rank-sum test was used to compare the expression level and module score, where *P* value<0.05 considered significantly different (*: $P<0.05$; ***: $P<0.001$). Two-sided asymptotic two-sample Kolmogorov-Smirnov test was used to compare the pseudotime distributions. Bonferroni-adjusted *P* value<0.01 was considered significantly different.

The experimental details can be found in Supplementary Methods.

Study approval

For human study, informed consent was obtained from all participants and the study was approved by the institutional review board of the University of Hong Kong and the Hospital Authority ((HKU/HA HKW IRB) UW 13-225). All animals were kept in the Animal

Laboratory of the University of Hong Kong, and all experiments were performed in accordance with procedures approved by the Committee on the Use of Live Animals, the University of Hong Kong (CULATR 23-493 and CULATR 23-029).

Data availability

Raw sequencing data for E15.5 and E13.5 mouse ENS from the scRNA-seq and the ST-seq data are deposited in the Sequence Read Archive under BioProjects PRJNA1295088, PRJNA752243 and PRJNA1006077, respectively. Processed data and code are accessible on Zenodo (https://doi.org/10.5281/zenodo.15979367) and GitHub (https://github.com/ellylab/Vcl-ENS). Public datasets used in this article can be downloaded from Gene Expression Omnibus using accession numbers GSE149524 and GSE186525. All data points shown in graphs are available in the Supporting Data Values file.

Author contributions:

L.L. and M.L. performed bioinformatics analyses under the supervision of E.S.W.N. and A.J., respectively. X.W. analyzed the mouse mutants. P.H.Y.C and K.K.Y.W. provided the clinical data. M.M.G.B. conducted the genetic analyses. P.L. and C.Y. performed in vitro studies. E.S.W.N. supervised the whole project. E.S.W.N. and L.L. prepared the manuscript.

Acknowledgments:

We thank Drs. Frank Lai, Pang Li, Kathy Lui, Reeson Wang, Kasey Lau and Miss Ophelia Liu for establishing the iCas-iPSC line, conducting some of the in vitro and live-imaging studies. Confocal imaging and RNA sequencing were performed using equipment maintained by the Li Ka Shing Faculty of Medicine Faculty Core and the Centre for PanorOmic Sciences, the University of Hong Kong, respectively. The work described in this paper was substantially

supported by seed funding from the University of Hong Kong and the GRF grants from the Research Grants Council of Hong Kong Special Administrative Region, China Hong Kong (HKU17111824 &17107322) to E.S.W.N.

References:

1. Montalva L, et al. Hirschsprung disease. *Nat Rev Dis Primers.* 2023;9(1):54.
2. Heanue TA, et al. Enteric nervous system development and Hirschsprung's disease: advances in genetic and stem cell studies. *Nat Rev Neurosci.* 2007;8(6):466-79.
3. Nagashimada M, et al. Autonomic neurocristopathy-associated mutations in PHOX2B dysregulate SOX10 expression. *J Clin Invest.* 2012;122(9):3145-58.
4. Anderson RB, et al. The cell adhesion molecule L1 is required for chain migration of neural crest cells in the developing mouse gut. *Gastroenterology.* 2006;130(4):1221-32.
5. Faure C, et al. Gangliogenesis in the enteric nervous system: Roles of the polysialylation of the neural cell adhesion molecule and its regulation by bone morphogenetic protein-4. *Dev Dynam.* 2007;236(1):44-59.
6. Fu M, et al. BMP signaling regulates murine enteric nervous system precursor migration, neurite fasciculation, and patterning via altered Ncam1 polysialic acid addition. *Dev Biol.* 2006;299(1):137-50.
7. Bays JL, et al. Vinculin in cell-cell and cell-matrix adhesions. *Cell Mol Life Sci.* 2017;74(16):2999-3009.
8. Thievessen I, et al. Vinculin-actin interaction couples actin retrograde flow to focal adhesions, but is dispensable for focal adhesion growth. *J Cell Biol.* 2013;202(1):163-77.
9. Plotnikov SV, et al. Force fluctuations within focal adhesions mediate ECM-rigidity sensing to guide directed cell migration. *Cell.* 2012;151(7):1513-27.
10. Case LB, et al. Molecular mechanism of vinculin activation and nanoscale spatial organization in focal adhesions. *Nat Cell Biol.* 2015;17(7):880-92.
11. Johnson RP, et al. An intramolecular association between the head and tail domains of vinculin modulates talin binding. *J Biol Chem.* 1994;269(17):12611-9.
12. Johnson RP, et al. F-actin binding site masked by the intramolecular association of vinculin head and tail domains. *Nature.* 1995;373(6511):261-4.
13. Chen H, et al. Coincidence of actin filaments and talin is required to activate vinculin. *J Biol Chem.* 2006;281(52):40389-98.
14. Biswas R, et al. Mechanical instability of adherens junctions overrides intrinsic quiescence of hair follicle stem cells. *Dev Cell.* 2021;56(6):761-+.
15. Zemljic-Harpf AE, et al. Heterozygous inactivation of the vinculin gene predisposes to stress-induced cardiomyopathy. *Am J Pathol.* 2004;165(3):1033-44.
16. Marg S, et al. The vinculin-DeltaIn20/21 mouse: characteristics of a constitutive, actin-binding deficient splice variant of vinculin. *PLoS One.* 2010;5(7):e11530.
17. Lai FP, et al. Correction of Hirschsprung-Associated Mutations in Human Induced Pluripotent Stem Cells Via Clustered Regularly Interspaced Short Palindromic Repeats/Cas9, Restores Neural Crest Cell Function. *Gastroenterology.* 2017;153(1):139-53 e8.
18. Gui H, et al. Whole exome sequencing coupled with unbiased functional analysis reveals new Hirschsprung disease genes. *Genome Biol.* 2017;18(1):48.
19. Tang CS, et al. Identification of Genes Associated With Hirschsprung Disease, Based on Whole-Genome Sequence Analysis, and Potential Effects on Enteric Nervous System Development. *Gastroenterology.* 2018;155(6):1908-22 e5.
20. Druckenbrod NR, et al. Behavior of enteric neural crest-derived cells varies with respect to the migratory wavefront. *Dev Dyn.* 2007;236(1):84-92.
21. Chevalier NR, et al. A neural crest cell isotropic-to-nematic phase transition in the developing mammalian gut. *Commun Biol.* 2021;4(1):770.

22. Lake JI, et al. Enteric nervous system development: migration, differentiation, and disease. *Am J Physiol Gastrointest Liver Physiol.* 2013;305(1):G1-24.
23. Shi J, et al. Transgelin-2 contributes to proliferation and progression of hepatocellular carcinoma via regulating Annexin A2. *Biochemical and Biophysical Research Communications.* 2020/03/12;523(3).
24. Schaffer AE, et al. Biallelic loss of human CTNNA2, encoding alphaN-catenin, leads to ARP2/3 complex overactivity and disordered cortical neuronal migration. *Nat Genet.* 2018;50(8):1093-101.
25. RD Y, et al. Rap1 mediates sustained MAP kinase activation induced by nerve growth factor - PubMed. *Nature.* 04/09/1998;392(6676).
26. Li Z, et al. Transcriptomics of Hirschsprung disease patient-derived enteric neural crest cells reveals a role for oxidative phosphorylation. *Nat Commun.* 2023;14(1):2157.
27. Lu KV, et al. Differential Induction of Glioblastoma Migration and Growth by Two Forms of Pleiotrophin. *Journal of Biological Chemistry.* 2005/07/22;280(29).
28. Polykratis A, et al. Characterization of Heparin Affin Regulatory Peptide Signaling in Human Endothelial Cells. *Journal of Biological Chemistry.* 2005/06/10;280(23).
29. Olson TM, et al. Metavinculin mutations alter actin interaction in dilated cardiomyopathy. *Circulation.* 2002;105(4):431-7.
30. Vasile VC, et al. A missense mutation in a ubiquitously expressed protein, vinculin, confers susceptibility to hypertrophic cardiomyopathy. *Biochem Biophys Res Commun.* 2006;345(3):998-1003.
31. Graneli C, et al. Histopathological dimensions differ between aganglionic and ganglionic bowel wall in children with Hirschsprung's disease. *BMC Pediatr.* 2022;22(1):723.
32. Broders-Bondon F, et al. N-cadherin and β1-integrins cooperate during the development of the enteric nervous system. *Dev Biol.* 2012;364(2):178-91.
33. Wang RX, et al. Vinculin mediates a dynamic signal flow underlying cardiac outflow tract development as revealed by single-cell and spatial transcriptomic analysis. *J Adv Res.* 2025.
34. Papadimitriou E, et al. On the role of pleiotrophin and its receptors in development and angiogenesis. *International Journal of Developmental Biology.* 2022;66(1-3):115-24.
35. Polykratis A, et al. Characterization of heparin affin regulatory peptide signaling in human endothelial cells. *Journal of Biological Chemistry.* 2005;280(23):22454-61.
36. Zhou BY, et al. Identification of signaling pathways that specify a subset of migrating enteric neural crest cells at the wavefront in mouse embryos. *Dev Cell.* 2024;59(13).
37. Li G, et al. PTEN deletion leads to up-regulation of a secreted growth factor pleiotrophin. *J Biol Chem.* 2006;281(16):10663-8.
38. Li YS, et al. Pleiotrophin gene expression is highly restricted and is regulated by platelet-derived growth factor. *Biochem Biophys Res Commun.* 1992;184(1):427-32.
39. Tang CS, et al. Uncovering the genetic lesions underlying the most severe form of Hirschsprung disease by whole-genome sequencing. *Eur J Hum Genet.* 2018;26(6):818-26.
40. Li MX, et al. A comprehensive framework for prioritizing variants in exome sequencing studies of Mendelian diseases. *Nucleic Acids Res.* 2012;40(7):e53.
41. Gonzalez F, et al. An iCRISPR Platform for Rapid, Multiplexable, and Inducible Genome Editing in Human Pluripotent Stem Cells. *Cell Stem Cell.* 2014;15(2):215-26.
42. DeKelver RC, et al. Functional genomics, proteomics, and regulatory DNA analysis in isogenic settings using zinc finger nuclease-driven transgenesis into a safe harbor locus in the human genome. *Genome Research.* 2010;20(8):1133-42.

43. Lau ST, et al. Activation of Hedgehog Signaling Promotes Development of Mouse and Human Enteric Neural Crest Cells, Based on Single-Cell Transcriptome Analyses. *Gastroenterology.* 2019;157(6):1556-71 e5.
44. Li P, et al. alphaE-catenin inhibits a Src-YAP1 oncogenic module that couples tyrosine kinases and the effector of Hippo signaling pathway. *Genes Dev.* 2016;30(7):798-811.
45. Liu JA, et al. Identification of GLI Mutations in Patients With Hirschsprung Disease That Disrupt Enteric Nervous System Development in Mice. *Gastroenterology.* 2015;149(7):1837-48.e5.

Figure legends:

Figure 1. HSCR-associated mutations in *VCL* interrupt focal adhesion (FA) assembly. (A) The schematic shows that mutations affect different functional domains of the VCL protein. **(B)** Immunofluoresecent stains show the FAs as marked by colocalization of Paxillin and Vinculin in HeLa cells overexpressing various *VCL* mutants. **(C)** Bar chart shows the average FA size found in cells overexpressing various *VCL* mutants (mean±SEM, >50 cells were analyzed; ***: $P<0.001$, ONE-way ANOVA). Co-Immunoprecipitation assay indicates that M209L substitution in VCL **(D)** enhances head and tail interaction, **(E)** leading to reduced binding affinity to phosphorylated paxillin.

Figure 2. Malformation of enteric ganglia in *Vcl* cKO at E18.5. (A) Three regions (proximal: C1; middle: C2 and distal: C3) of colon were collected from control and *Vcl* mutants (*Vcl* $KO^{Wnt1\text{-}Cre}$) for whole-mount acetylcholinesterase (AchE) staining. **(B)** Whole-mount immunofluorescence of TUJ1, HuD and SOX10 shows ENS network in the distal colon of E18.5 *Vcl* cKO was aberrantly organised. **(C)** Magnified images of the regions highlighted in the red dotted boxes in (B). The percentages of neurons (HuD^+) and glia ($SOX10^+$) normalized to the total number of cells ($DAPI^+$) and the relative neuron-to-glia ratio in each region are shown in the bar charts. (mean±SEM, n: number of embryonic guts analyzed, $P<0.05$ was considered significantly different, ***: $P<0.001$, Student *t*-test, 2-tailed). 6-8 randomly selected regions were analyzed.

Figure 3. Immature ENS in *Vcl* cKO at E18.5. Immunofluorescence of **(A)** PHOX2B & SOX10; and **(B)** SMA and YFP counterstained with DAPI on cross-sections of E18.5 distal colon and the quantitative data are shown in bar charts. (mean±SEM, n: number of embryonic guts analyzed, $P<0.05$ was considered significantly different, ***: $P<0.001$, Student *t*-test, 2-tailed). 6-8 randomly selected regions were analyzed. Mes: mesenchyme; e: endoderm; lu: lumen; ci: circumferential muscle; ol: outer longitudinal layer; il: inner longitudinal layer; m.p.: myenteric plexus.

Figure 4. Failure to form the migration chain in *Vcl* mutants. (A) The migration of ENCCs in hindgut and colonization in cecum were examined at E11.5. White dashed lines indicate the migration distance. Bar chart shows significantly delayed migration of ENCCs in the mutant mice. *P* value less than 0.05 was considered significantly different and marked by "*", Student

t-test, 2-tailed. **(B)** Time-lapse images from live imaging of ENCC migration in E12.5 embryonic guts, where YFP-labelled ENCCs located at the migratory wavefront (asterisks) were tracked and their migratory paths were indicated by arrows. Bar chart shows the net speed of migration. **(C)** Whole mount immunofluorescence of YFP-labelled ENCCs in E13.5 hindguts. Failure in formation of migratory chains and presence of solitary ENCCs (arrowheads) were observed in *Vcl* cKO. *P* value less than 0.5 was considered significantly different and marked by "**", Student *t*-test, 2-tailed.

Figure 5. scRNA-seq analysis revealed a delayed progression of *Vcl* mutant cells along the neuronal lineage differentiation trajectory. (A) The workflow summarizing scRNA-seq data analysis and corresponding functional validations. **(B)** The integrated UMAP (Uniform Manifold Approximation and Projection) projection of 30,157 cells ENCCs at E13.5 and E15.5, colored by cell types. (BP, biopotent progenitor; GP, glial progenitor; Branch A & Branch B neurons, annotated by integrating the data from Mikhailova et al. 2021[1]; ENMFB, enteric mesothelial fibroblast. **(C)** The expression of marker genes and proliferative markers across cell types. **(D)** The proportion of cell types across different samples. Empirical Bayes moderated T-test is used for the cell proportion comparison, with Benjamini-Hochberg-adjusted *P* value<0.05 considered significant. The proportion of E13.5 BP, E13.5 Branch A and E15.5 Branch A neurons is affected. **(E)** Comparison of RNA velocity in control and *Vcl* mutant. **(F)** The density plot shows the distributions of pseudotime of cell states inferred by Slingshot, revealing a delayed differentiation of neurons. **(G)** Expression of Branch A markers in control and *Vcl* mutant. Two-sided Wilcoxon rank-sum test, ****: *P*<0.0001.

Figure 6. Increased progenitor cells and delayed differentiation in *Vcl* mutants. (A) Mitotic ENS neurons ($Ki67^+PHOX2B^+YFP^+$); **(B)** mature (HuD^+SOX10^-) and immature (HuD^+SOX10^+) neurons; and **(C)** inhibitory ($nNOS^+$) neurons. Bar charts show the quantitative data (mean±SEM, n: number of embryonic guts analyzed, *P*<0.05 was considered significantly different, *: *P*<0.05 ; ***: *P*<0.001, Student *t*-test, two-tailed).

Figure 7. Disrupted gene regulatory network and pathways in BP-to-Branch A lineage. (A) The density plot shows the pseudotime distributions of four disrupted cell states. E13.5 BP, E15.5 Neuroblast, E13.5 Branch A neurons and E15.5 Branch A neurons. **(B)** Gene regulatory network of the DEGs along the BP-to-Branch A lineage, colored by regulatory modules defined by regulatory relationship (Module1, genes regulated by E2f1 and Egr1;

Module2, genes regulated by Egr1 only; Module3, genes regulated by Egr1 and Klf7; Module4, genes regulated by Klf7 only). Lines connecting *Vcl* represent the potential regulation and known protein-protein interactions from the STRING database. **(C)** The boxplot shows the module score in the corresponding disrupted cell states. **(D)** The dot plot shows the Spearman correlation on the expression of *Vcl* and genes in modules. The top 10 genes ranked by correlation are labelled and shown in (B). The dot plots show **(E)** the biological processes enriched by the genes in the modules and **(F)** KEGG pathways enriched by the DEGs identified in Neuroblast and BranchA neurons.

Figure 8. VCL is implicated in multiple stages of neuronal lineage differentiation of ENS cells. (A) Schematic shows the human iPSC-based model of ENS development. An inducible-iPSC line was used, where the addition of doxycycline induced the expression of Cas9. Co-transfection of *VCL*-specific gRNA drove the deletion of *VCL* gene in FACS-enriched ENCCs (Day 12) or ENCCs committed to the neuronal lineage (Day 15). Immunocytochemistry with antibodies against pan-neuronal markers (NF and PGP9.5) on cells with *VCL* knock-down on **(B)** day 12 and **(C)** day 15. Bar charts show the percentage of neurons marked by NF or PGP9.5 over the total number of $DAPI^+$ cells. Data shown in the bar charts are mean +/- SEM from 3 independent experiments. *P* value less than 0.05 was considered significantly different. Student *t*-test, 2-tailed. **(D)** Western blot analyses of ITGB1, MAPK, phospho-MAPK and VCL. ACTIN was used as the loading control. The relative expression levels were shown in the bar charts (mean +/- SEM from 3 independent experiments). *P* value less than 0.05 was considered significantly different. Student *t*-test, 2-tailed.

Figure 9. Disrupted cell-cell interactions in *Vcl* cKO revealed by spatial transcriptomics of embryonic guts at E13.5. (A) The spatial annotation of the selected regions of the large intestine at E13.5. (EPI, epithelial; MES, mesenchymal cells; NC, neural crest cells.) **(B)** Bar charts illustrate the total number and strength of NC-related cell-cell interactions. **(C)** The number and strength of NC-related interactions across different pathways are presented. **(D)** The top three disrupted cell-cell interactions in each group, ranked by probability. All of these interactions are entirely abolished in the mutant within the corresponding cell-type pairs.

Figure 10. Down-regulation of PTN, ITGB1 and CADH2 in *Vcl*-deficient ENS at E18.5. Immunohistochemistry using antibodies against **(A)** PTN; **(B)** ITGB1; and **(C)** N-CADHERIN in the E18.5 distal colon of control and *Vcl* cKO mutants. ENS cells were YFP-labeled. **(D)** A

Western blot was conducted with whole gut lysate from control and mutants. The relative CADH2 expression levels are shown compared to the control. GAPDH served as the loading control.

Figure 11. Dynamic expression of PTN in ENS and mesenchyme is essential for the formation of the muscle layer of the gut. (A) Immunohistochemistry of PTN in E13.5, E15.5 & E18.5 of control (*Wnt1-Cre; Rosa26*^{YFP}) and *Vcl* cKO (*Vcl* KO$^{Wnt1\text{-}Cre}$) guts. **(B)** Whole-mount acetylcholinesterase (AchE) staining of control and *Ptn* KO colon. **(C)** Whole-mount immunofluorescence of TUJ1, HuD and SOX10 shows ENS network aberrantly organized in the distal colon of E18.5 *Ptn* mutant. The average neuron-to-glia ratio in the 4-5 selected regions of distal colon is shown in the bar charts. Immunofluorescence of **(D)** PHOX2B & SOX10 and **(E)** Ki67 counterstained with DAPI on cross-sections of E18.5 distal colon. **(F)** Immunofluorescence staining for Calponin (red) and counterstained nuclei with DAPI (blue) in E15.5 Control (*Ptn*$^{+/+}$) and *Ptn*$^{-/-}$ colons. m.p.: myenteric plexus; Lu: lumen; lamina muscularis interna (yellow arrowhead) and the lamina muscularis externa (green arrowhead). Bar charts show the quantitative data. (mean±SEM, n: number of embryonic guts analyzed, $P<0.05$ was considered significantly different, *: $P<0.05$; ***: $P<0.001$, Student *t*-test, two-tailed).

Mutant	Exon	DNA alternation	Type	Functional domain	FA size	No. of patient	Patient phenotypes
I20T	Exon 1	59T>C	Missense	Vh1	NC	1	S-HSCR
M209L	Exon 6	625A>T	Missense	Vh1	↓↓	3	S-HSCR + VSD
A376G	Exon 9	1127C>G	Missense	Vh2	NC	1	S-HSCR
P398S	Exon 10	1192C>T	Missense	Vh2	↓	1	S-HSCR
K666N	Exon 14	1998G>T	Missense	Vh3	↓	1	S-HSCR
R1039Q	Exon 21	3116G>A	Missense	T5	↓	1	S-HSCR

Table 1. A summary of *VCL* mutations identified in HSCR patients and their impacts on FA size. FA: focal adhesion; NC: no change; ↓: reduction.

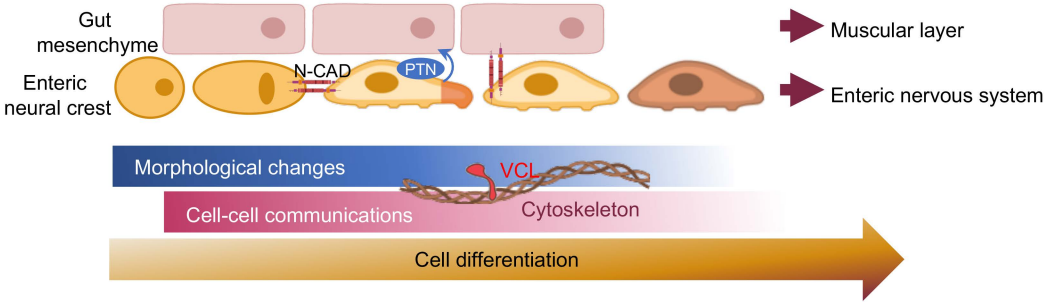
Gut
mesenchyme
Enteric
neural crest
N-CAD
PTN
Muscular layer
Enteric nervous system
Morphological changes
VCL
Cell-cell communications
Cytoskeleton
Cell differentiation

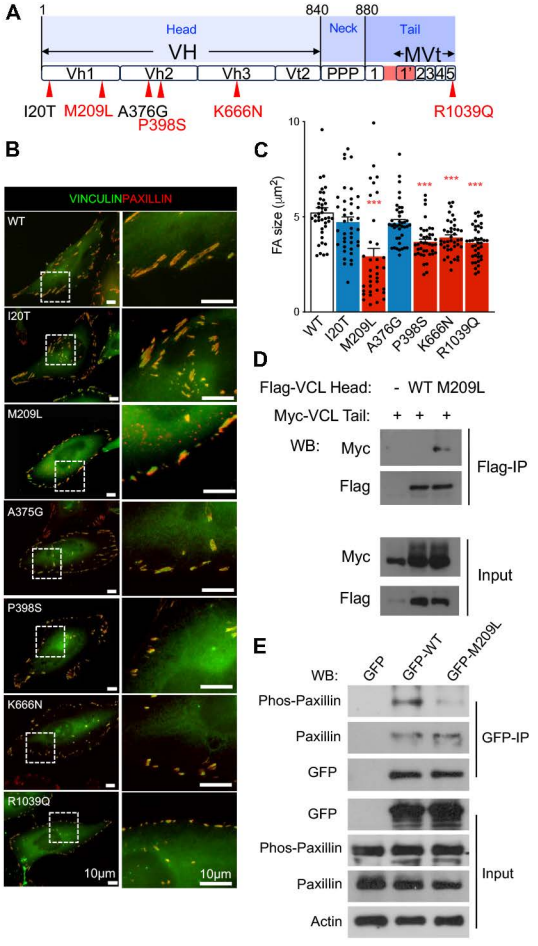
A
1
840
880
Head
Neck
Tail
VH
MVt
Vh1
Vh2
Vh3
Vt2
PPP
1
1'
2
3
4
5
I20T
M209L
A376G
P398S
K666N
R1039Q
B
VINCULIN
PAXILLIN
WT
I20T
M209L
A375G
P398S
K666N
R1039Q
10μm
10μm
C
FA size (μm²)
10
5
0
***
***
***
***
WT
I20T
M209L
A376G
P398S
K666N
R1039Q
D
Flag-VCL Head:
- WT M209L
Myc-VCL Tail:
+ + +
WB:
Myc
Flag
Flag-IP
Myc
Flag
Input
E
WB:
GFP
GFP-WT
GFP-M209L
Phos-Paxillin
Paxillin
GFP
GFP-IP
GFP
Phos-Paxillin
Paxillin
Actin
Input

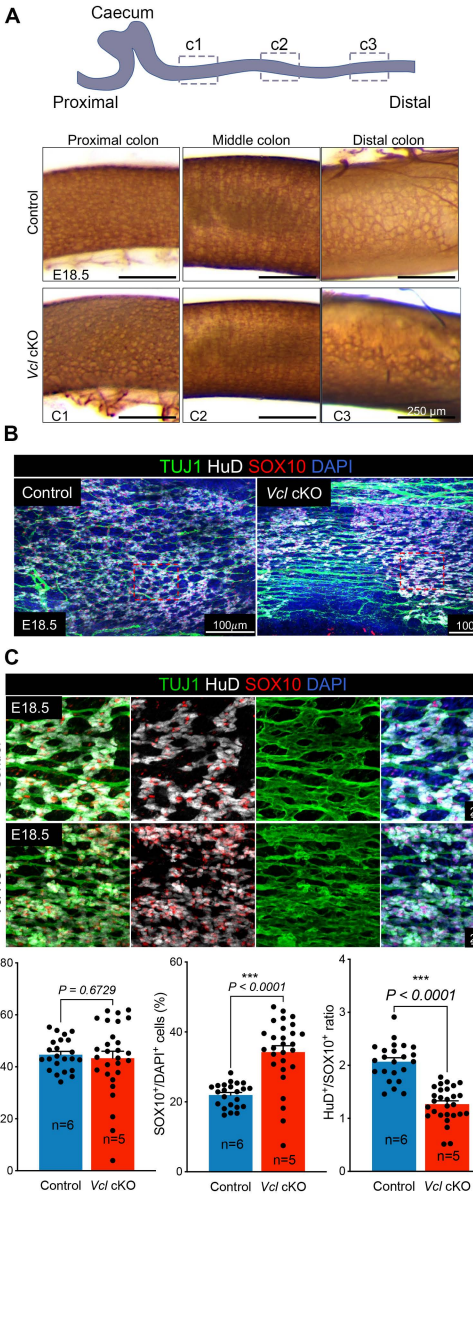
A
Caecum
c1
c2
c3
Proximal
Distal
Proximal colon
Middle colon
Distal colon
Control
E18.5
Vcl cKO
C1
C2
C3
250 μm
B
TUJ1 HuD SOX10 DAPI
Control
Vcl cKO
E18.5
100μm
C
TUJ1 HuD SOX10 DAPI
E18.5
Control
Vcl KO
25μm
HuD+/DAPI+ cells (%)
P = 0.6729
n=6
n=5
Control
Vcl cKO
SOX10+/DAPI+ cells (%)
***
P < 0.0001
HuD+/SOX10+ ratio

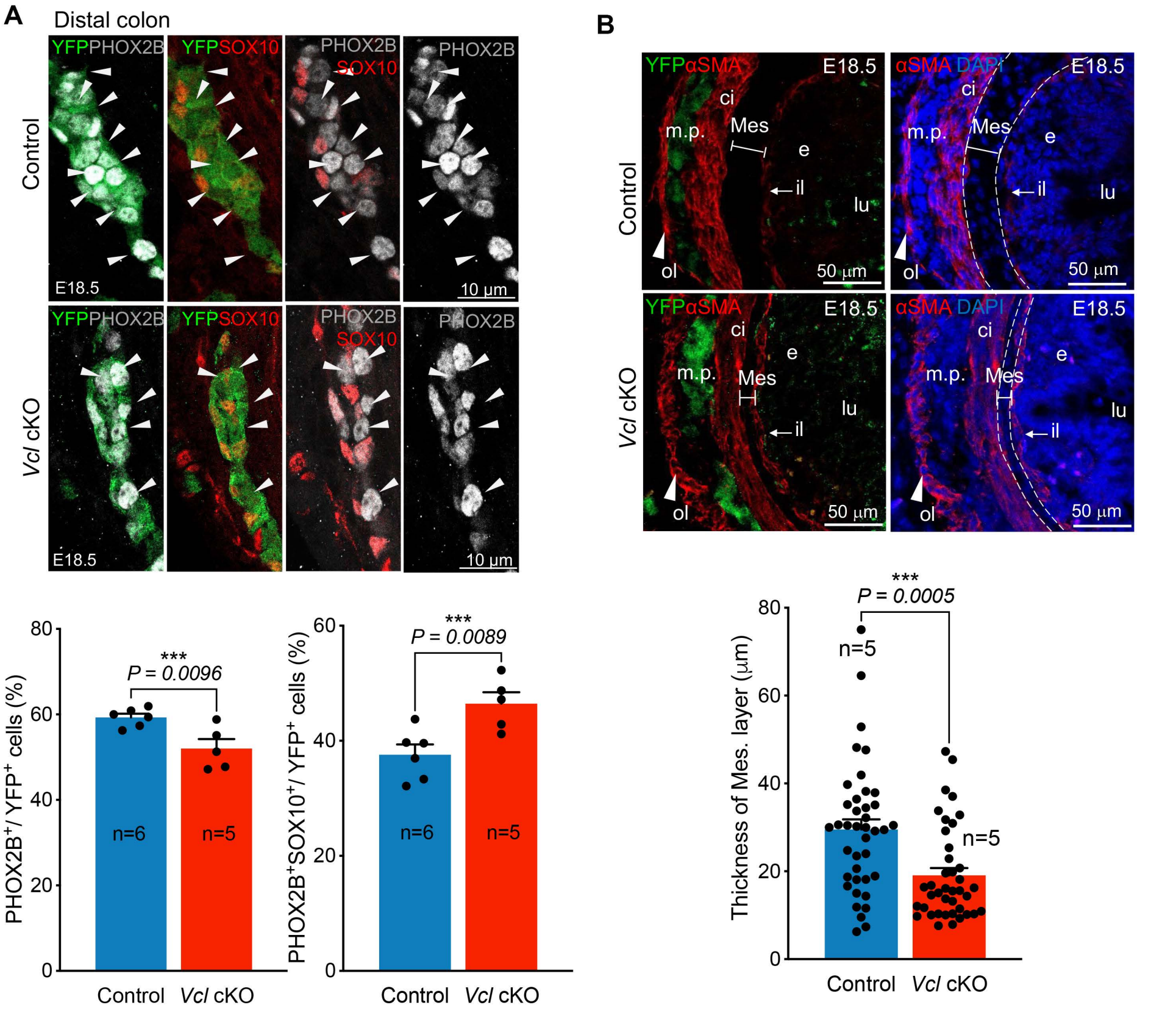
A
Distal colon
Control
Vcl cKO
YFPPHOX2B
YFPSOX10
PHOX2B
SOX10
E18.5
10 μm
B
YFPαSMA
αSMA DAPI
ci
m.p.
Mes
e
il
lu
ol
50 μm
PHOX2B+/ YFP+ cells (%)
***
P = 0.0096
n=6
n=5
Control
Vcl cKO
PHOX2B+SOX10+/ YFP+ cells (%)
***
P = 0.0089
Thickness of Mes. layer (μm)
***
P = 0.0005

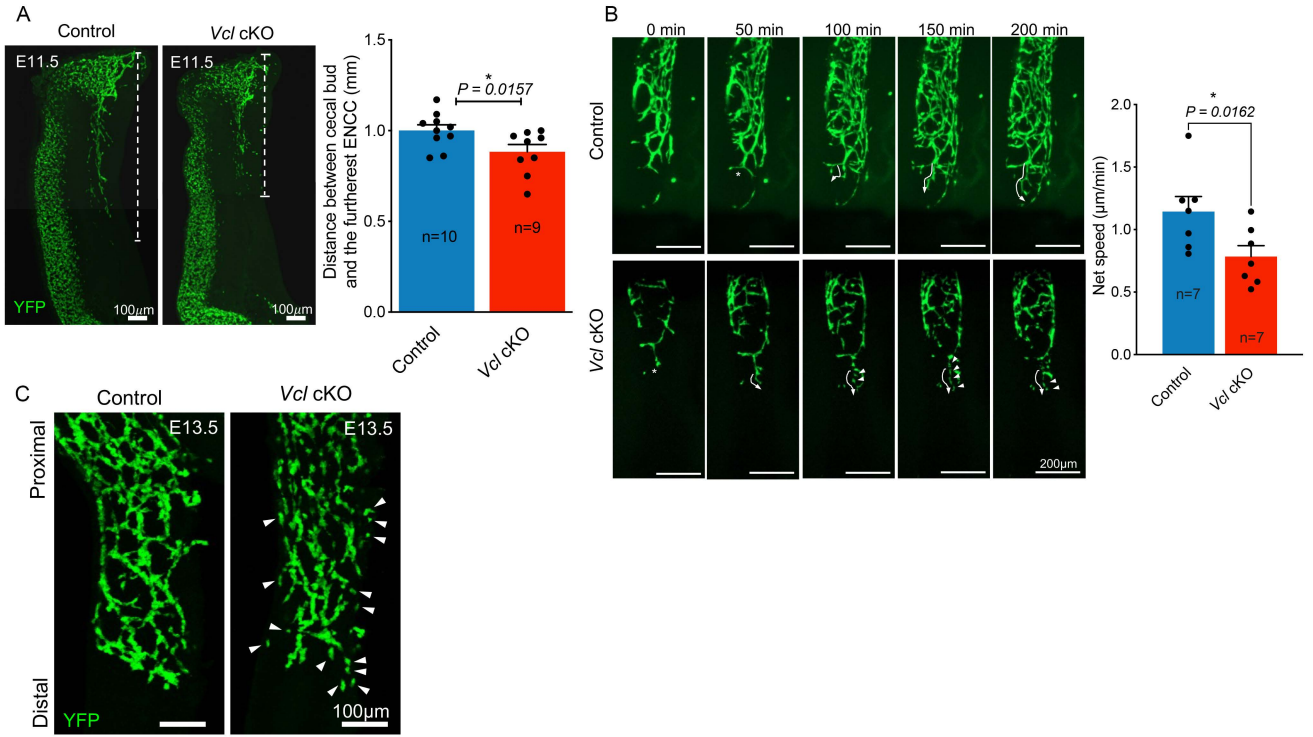
A
Control
Vcl cKO
E11.5
E11.5
YFP
100μm
100μm
Distance between cecal bud and the furtherest ENCC (mm)
1.5
1.0
0.5
0.0
*
P = 0.0157
n=10
n=9
Control
Vcl cKO
B
0 min
50 min
100 min
150 min
200 min
Control
Vcl cKO
200μm
Net speed (μm/min)
2.0
1.5
1.0
0.5
0.0
*
P = 0.0162
n=7
n=7
Control
Vcl cKO
C
Control
Vcl cKO
Proximal
Distal
E13.5
E13.5
YFP
100μm

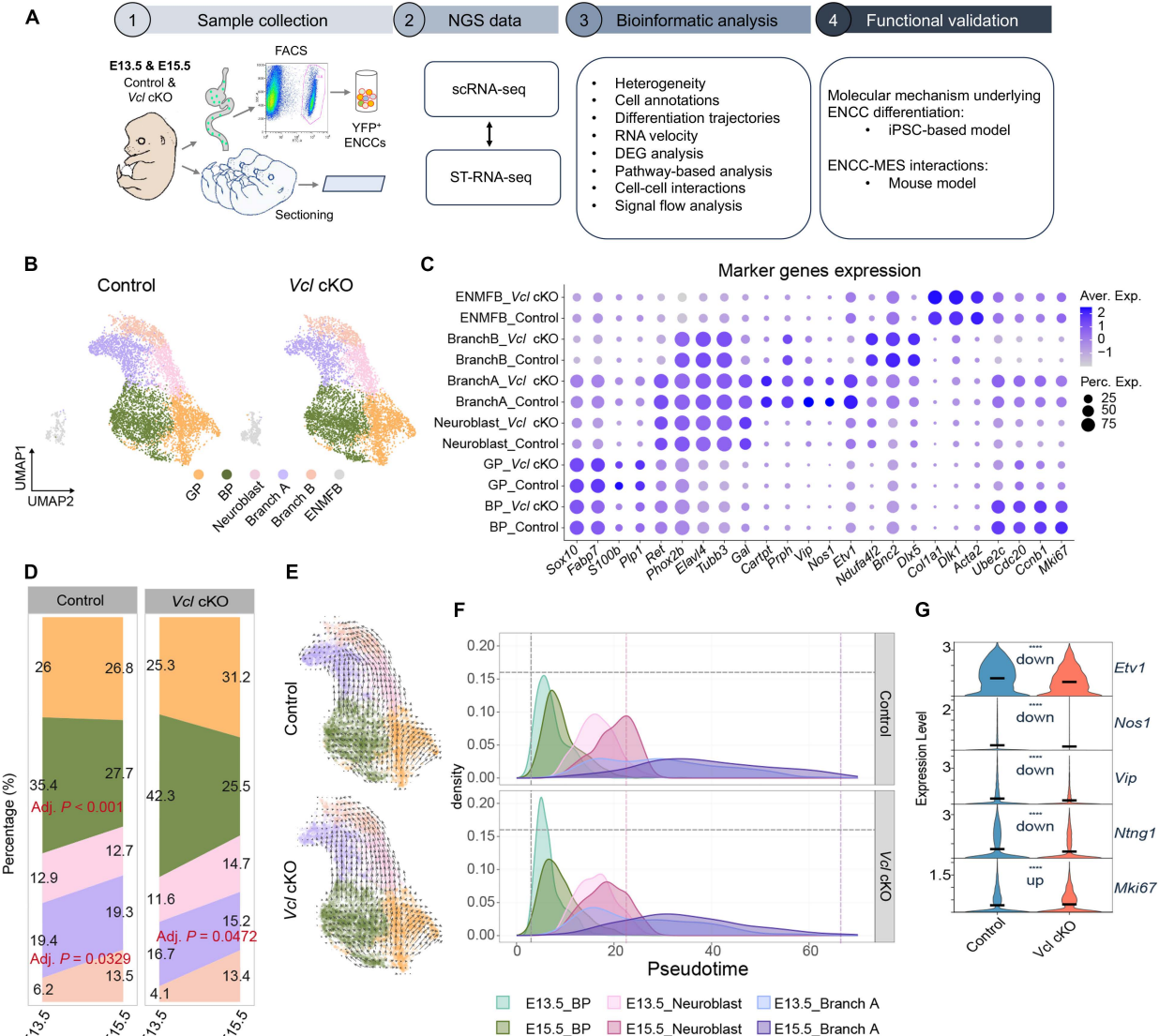
A
1 Sample collection
2 NGS data
3 Bioinformatic analysis
4 Functional validation
E13.5 & E15.5
Control &
Vcl cKO
FACS
YFP+
ENCCs
Sectioning
scRNA-seq
ST-RNA-seq
Heterogeneity
Cell annotations
Differentiation trajectories
RNA velocity
DEG analysis
Pathway-based analysis
Cell-cell interactions
Signal flow analysis
Molecular mechanism underlying ENCC differentiation:
iPSC-based model
ENCC-MES interactions:
Mouse model
B
Control
Vcl cKO
UMAP1
UMAP2
GP
BP
Neuroblast
Branch A
Branch B
ENMFB
C
Marker genes expression
ENMFB_Vcl cKO
ENMFB_Control
BranchB_Vcl cKO
BranchB_Control
BranchA_Vcl cKO
BranchA_Control
Neuroblast_Vcl cKO
Neuroblast_Control
GP_Vcl cKO
GP_Control
BP_Vcl cKO
BP_Control
Sox10
Fabp7
S100b
Plp1
Ret
Phox2b
Elavl4
Tubb3
Gal
Cartpt
Prph
Vip
Nos1
Etv1
Ndufa4l2
Bnc2
Dlx5
Col1a1
Dlk1
Acta2
Ube2c
Cdc20
Ccnb1
Mki67
Aver. Exp.
2
1
0
−1
Perc. Exp.
25
50
75
D
Control
Vcl cKO
Percentage (%)
26
26.8
35.4
27.7
12.7
12.9
19.3
19.4
13.5
6.2
Adj. P < 0.001
Adj. P = 0.0329
25.3
31.2
42.3
25.5
14.7
11.6
15.2
16.7
13.4
4.1
Adj. P = 0.0472
E13.5
E15.5
E13.5
E15.5
E
Control
Vcl cKO
F
density
0.20
0.15
0.10
0.05
0.00
Control
Vcl cKO
0
20
40
60
Pseudotime
E13.5_BP
E13.5_Neuroblast
E13.5_Branch A
E15.5_BP
E15.5_Neuroblast
E15.5_Branch A
G
Expression Level
3
2
3
3
1.5
down
down
down
down
up
Etv1
Nos1
Vip
Ntng1
Mki67
Control
Vcl cKO

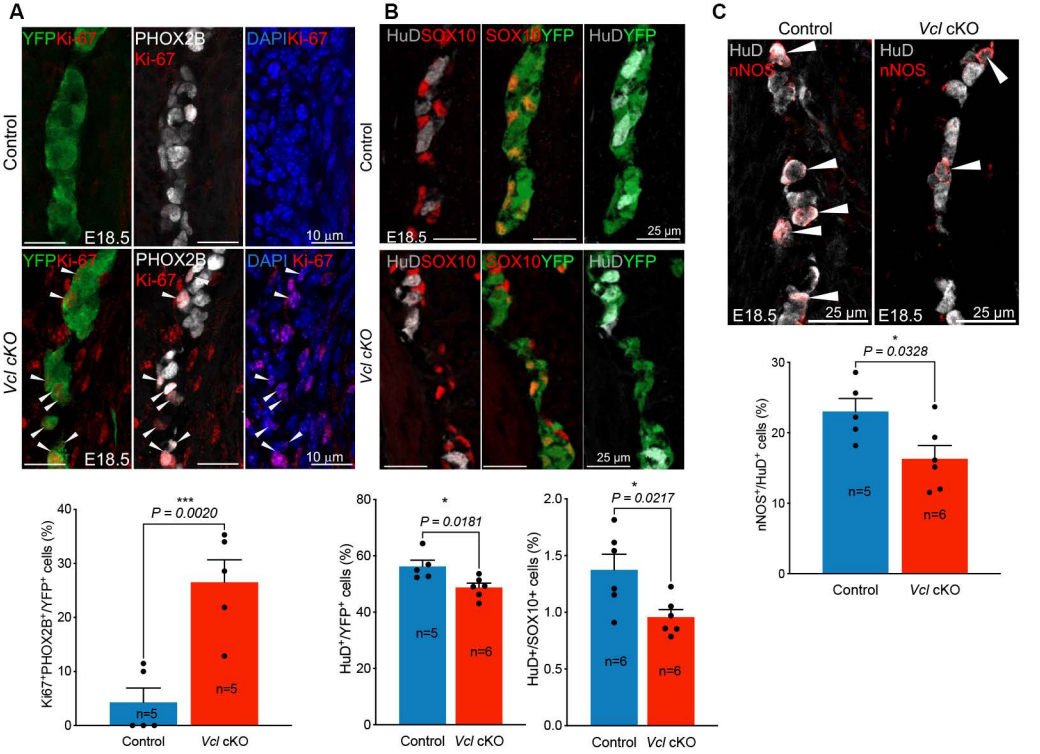
A
YFP Ki-67
PHOX2B Ki-67
DAPI Ki-67
Control
Vcl cKO
E18.5
10 μm
B
HuD SOX10
SOX10 YFP
HuD YFP
Control
Vcl cKO
E18.5
25 μm
C
Control
Vcl cKO
HuD
nNOS
E18.5
25 μm
Ki67+PHOX2B+/YFP+ cells (%)
***
P = 0.0020
n=5
n=5
HuD+/YFP+ cells (%)
*
P = 0.0181
n=5
n=6
HuD+/SOX10+ cells (%)
*
P = 0.0217
n=6
n=6
nNOS+/HuD+ cells (%)
*
P = 0.0328
n=5
n=6
Control
Vcl cKO

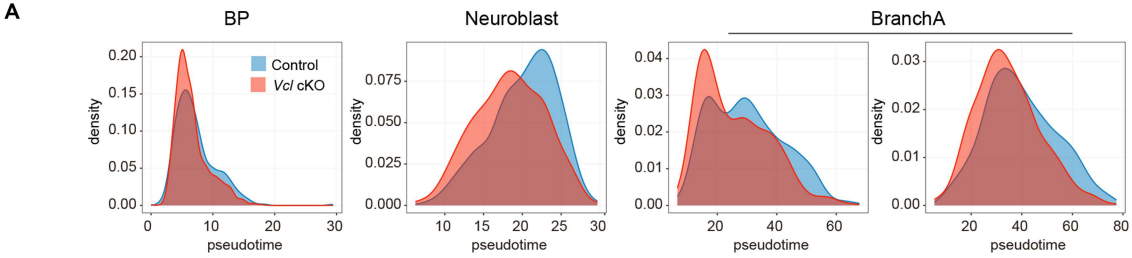
A
BP
Neuroblast
BranchA
Control
Vcl cKO
density
pseudotime

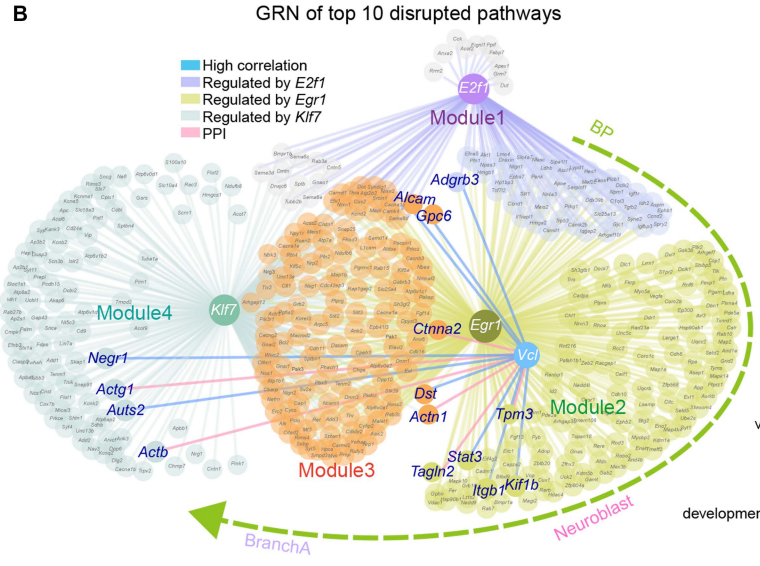
B
GRN of top 10 disrupted pathways
High correlation
Regulated by E2f1
Regulated by Egr1
Regulated by Klf7
PPI
Module1
Module2
Module3
Module4
BP
Neuroblast
BranchA
E2f1
Klf7
Egr1
Vcl
Adgrb3
Alcam
Gpc6
Ctnna2
Dst
Actn1
Tpm3
Stat3
Tagln2
Itgb1
Kif1b
Negr1
Actg1
Auts2
Actb

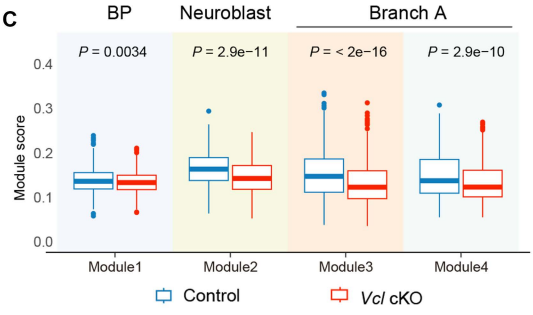
C
BP
Neuroblast
Branch A
P = 0.0034
P = 2.9e−11
P = < 2e−16
P = 2.9e−10
Module score
Module1
Module2
Module3
Module4
Control
Vcl cKO

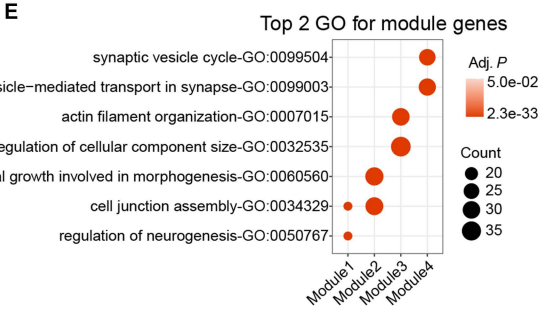
E
Top 2 GO for module genes
synaptic vesicle cycle-GO:0099504
vesicle−mediated transport in synapse-GO:0099003
actin filament organization-GO:0007015
regulation of cellular component size-GO:0032535
developmental growth involved in morphogenesis-GO:0060560
cell junction assembly-GO:0034329
regulation of neurogenesis-GO:0050767
Module1
Module2
Module3
Module4
Adj. P
5.0e-02
2.3e-33
Count
20
25
30
35

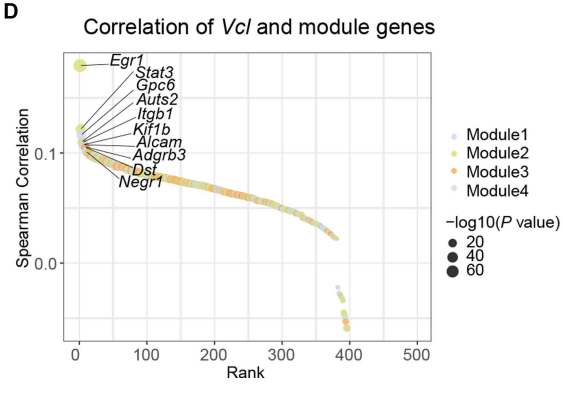
D
Correlation of Vcl and module genes
Egr1
Stat3
Gpc6
Auts2
Itgb1
Kif1b
Alcam
Adgrb3
Dst
Negr1
Spearman Correlation
Rank
Module1
Module2
Module3
Module4
−log10(P value)
20
40
60

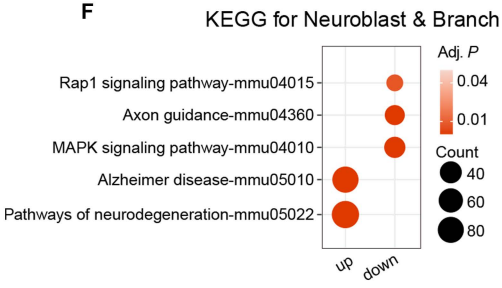
F
KEGG for Neuroblast & Branch A
Rap1 signaling pathway-mmu04015
Axon guidance-mmu04360
MAPK signaling pathway-mmu04010
Alzheimer disease-mmu05010
Pathways of neurodegeneration-mmu05022
up
down
Adj. P
0.04
0.01
Count
40
60
80

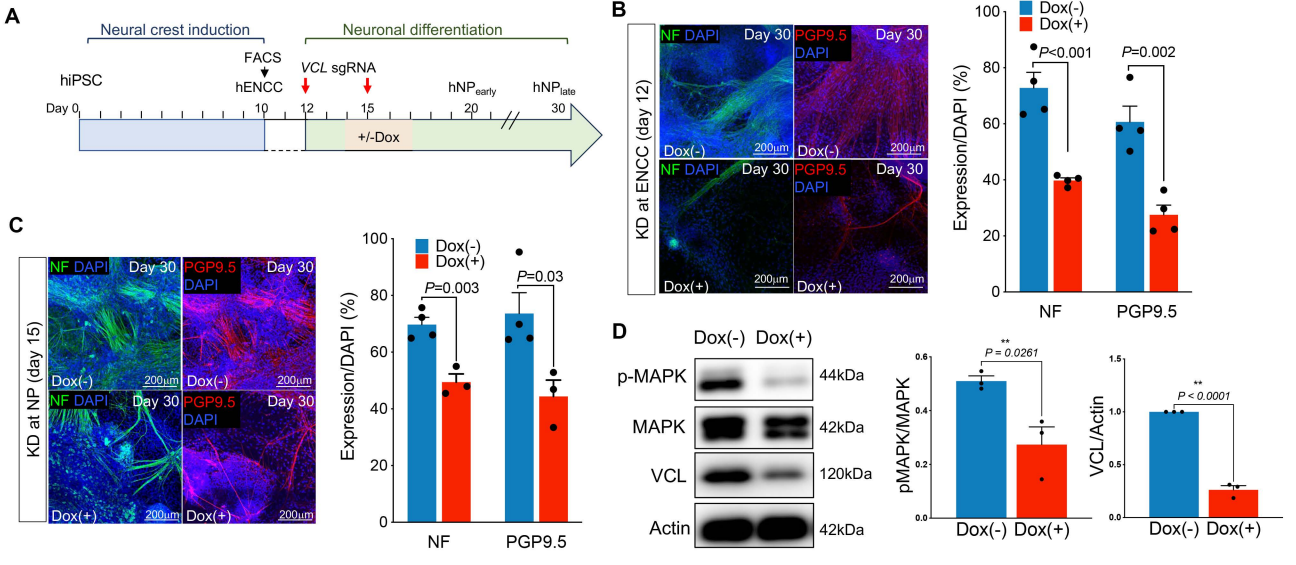
A
Neural crest induction
Neuronal differentiation
FACS
hiPSC
hENCC
VCL sgRNA
hNPearly
hNPlate
Day 0
10
12
15
20
30
+/-Dox
B
KD at ENCC (day 12)
NF DAPI
Day 30
PGP9.5
DAPI
Dox(-)
Dox(+)
200μm
Dox(-)
Dox(+)
Expression/DAPI (%)
P<0.001
P=0.002
NF
PGP9.5
C
KD at NP (day 15)
NF DAPI
Day 30
PGP9.5
DAPI
Dox(-)
Dox(+)
200μm
Expression/DAPI (%)
P=0.003
P=0.03
NF
PGP9.5
D
Dox(-)
Dox(+)
p-MAPK
MAPK
VCL
Actin
44kDa
42kDa
120kDa
42kDa
pMAPK/MAPK
P = 0.0261
VCL/Actin
P < 0.0001

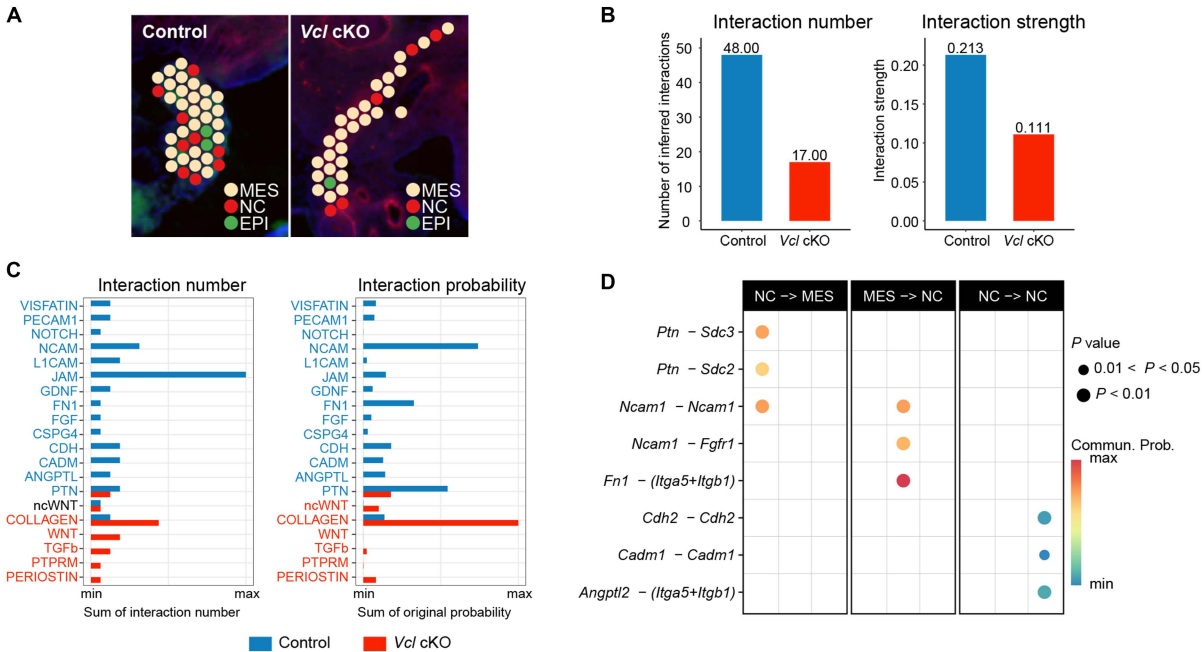
A
Control
Vcl cKO
MES
NC
EPI
MES
NC
EPI
B
Interaction number
Interaction strength
Number of inferred interactions
50
40
30
20
10
0
48.00
17.00
Control
Vcl cKO
Interaction strength
0.20
0.15
0.10
0.05
0.00
0.213
0.111
Control
Vcl cKO
C
Interaction number
Interaction probability
VISFATIN
PECAM1
NOTCH
NCAM
L1CAM
JAM
GDNF
FN1
FGF
CSPG4
CDH
CADM
ANGPTL
PTN
ncWNT
COLLAGEN
WNT
TGFb
PTPRM
PERIOSTIN
min
max
Sum of interaction number
Sum of original probability
Control
Vcl cKO
D
NC -> MES
MES -> NC
NC -> NC
Ptn – Sdc3
Ptn – Sdc2
Ncam1 – Ncam1
Ncam1 – Fgfr1
Fn1 – (Itga5+Itgb1)
Cdh2 – Cdh2
Cadm1 – Cadm1
Angptl2 – (Itga5+Itgb1)
P value
0.01 < P < 0.05
P < 0.01
Commun. Prob.
max
min

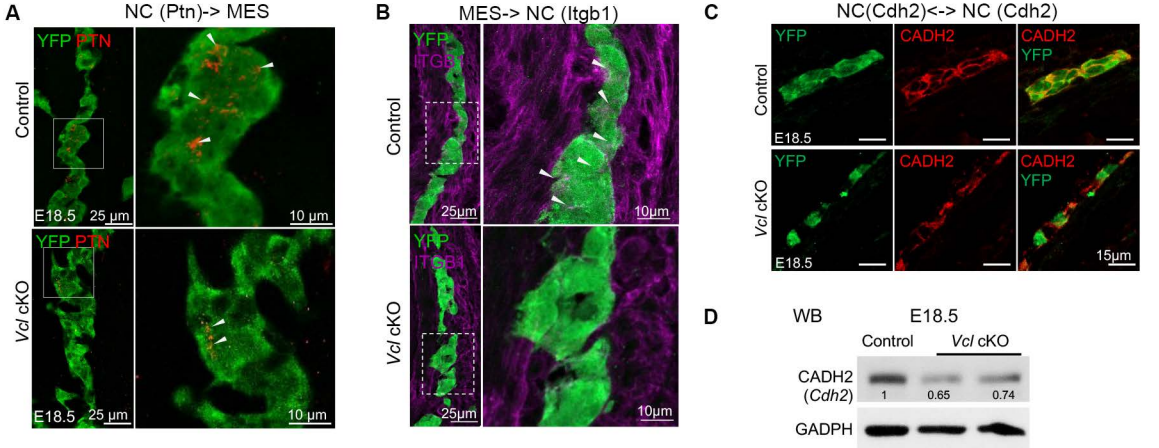
A
NC (Ptn)-> MES
YFP PTN
Control
E18.5
25 μm
10 μm
YFP PTN
Vcl cKO
E18.5
25 μm
10 μm
B
MES-> NC (Itgb1)
YFP
ITGB1
Control
25μm
10μm
YFP
ITGB1
Vcl cKO
25μm
10μm
C
NC(Cdh2)<-> NC (Cdh2)
YFP
CADH2
CADH2
YFP
Control
E18.5
YFP
CADH2
CADH2
YFP
Vcl cKO
E18.5
15μm
D
WB
E18.5
Control
Vcl cKO
CADH2
(Cdh2)
1
0.65
0.74
GADPH

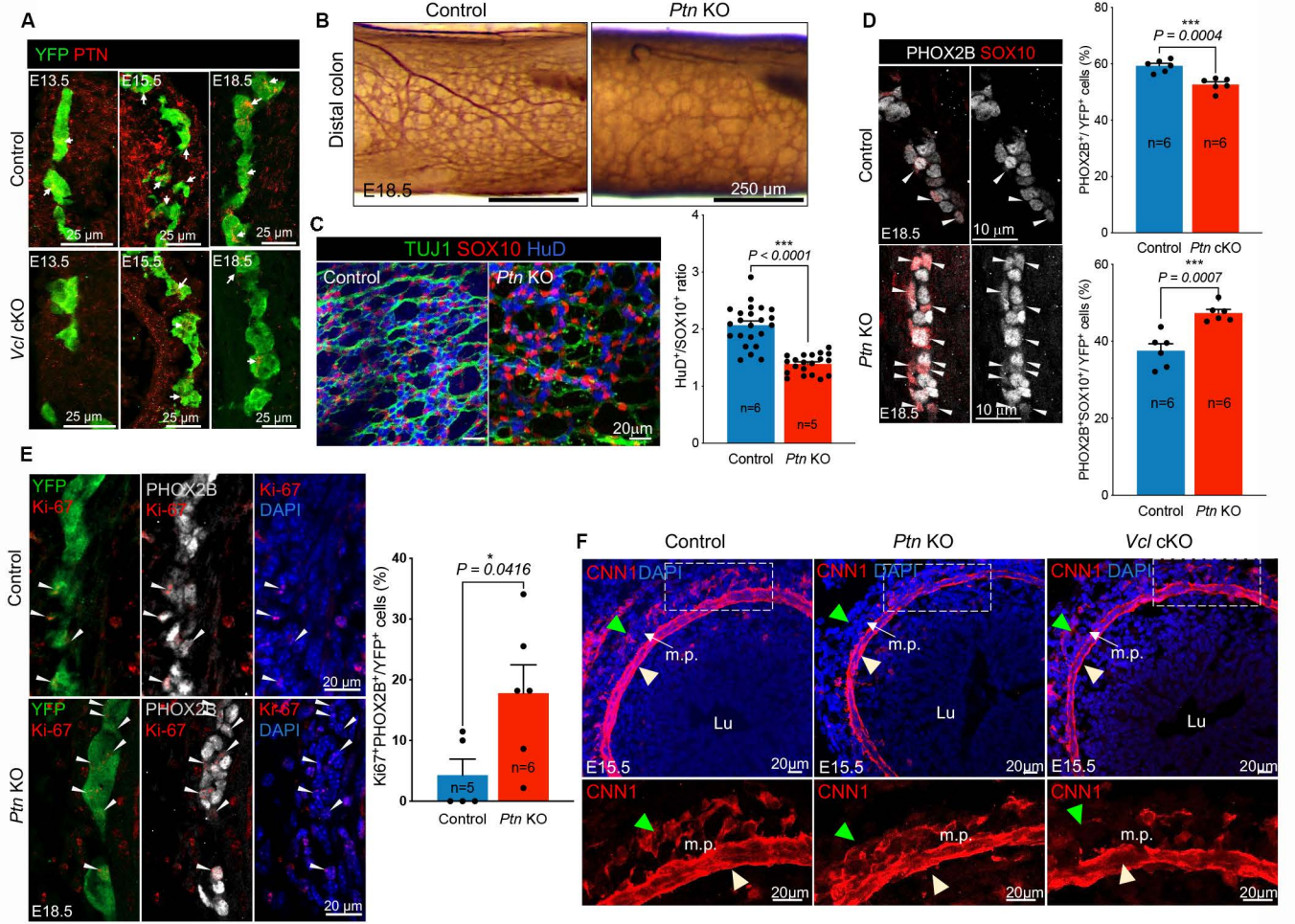
A
YFP PTN
E13.5
E15.5
E18.5
Control
Vcl cKO
25 μm
B
Control
Ptn KO
Distal colon
E18.5
250 μm
C
TUJ1 SOX10 HuD
Control
Ptn KO
20μm
HuD+/SOX10+ ratio
P < 0.0001
***
n=6
n=5
Control
Ptn KO
D
PHOX2B SOX10
Control
Ptn KO
E18.5
10 μm
PHOX2B+/YFP+ cells (%)
P = 0.0004
PHOX2B+SOX10-/YFP+ cells (%)
P = 0.0007
E
YFP
Ki-67
PHOX2B
DAPI
20 μm
Ki67+PHOX2B+/YFP+ cells (%)
P = 0.0416
*
F
Control
Ptn KO
Vcl cKO
CNN1 DAPI
m.p.
Lu
E15.5
20μm
CNN1

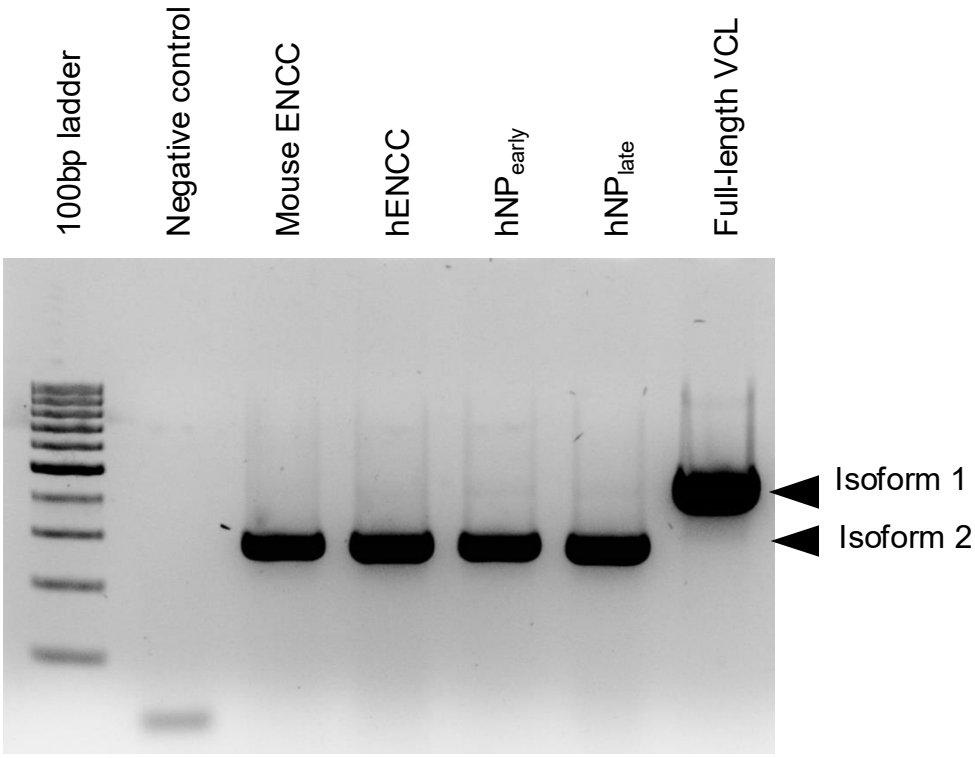

Supplementary Figure 1. Expression of *VCL* isoform 2 in mouse and human ENCCs. RT-PCR data show the expression of *Vcl* isoform 2, but not isoform 1, in mouse ENCCs, human iPSC-derived ENCCs, and their neuronal derivatives (hNP$_{early}$ and hNP$_{late}$: days 9 and day 20 of neuronal differentiation).

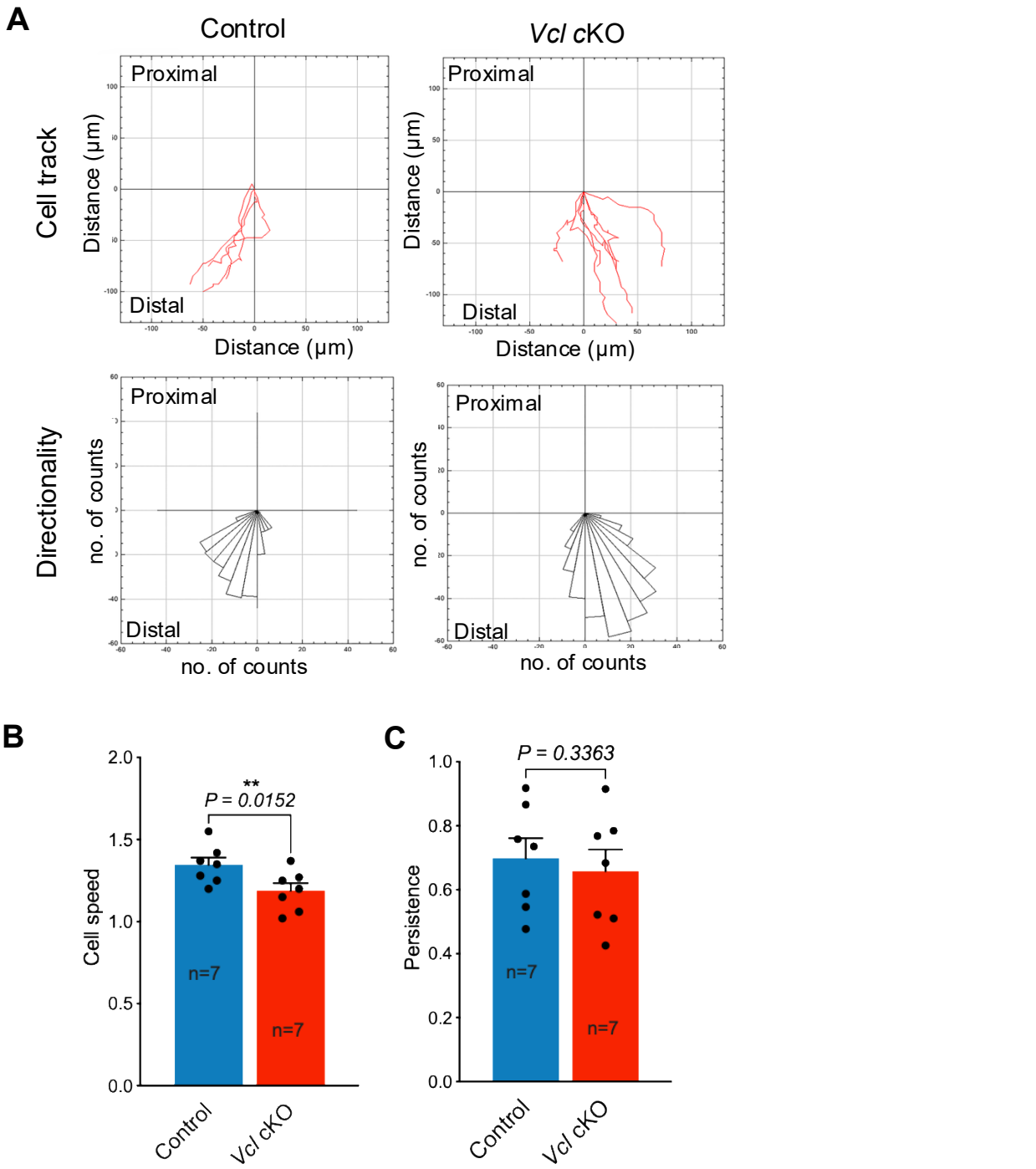

Supplementary Figure 2. Regular migratory trajectory and pattern found in *Vcl* cKO **(A**)Trajectory plot (upper panel) and polar histograms (lower panel) represent the trajectories of the most caudal cell at 10-minute intervals in 3 explants of E12.5 hindgut. ENCCs in both *Vcl* cKO and control showed a uniform tendency to migrate distally. Bar plots show the **(B) c**ell speed at which the migratory wave front of ENCCs migrated caudally along the gut and **(C)** persistence of control and *Vcl* null ENS cells.

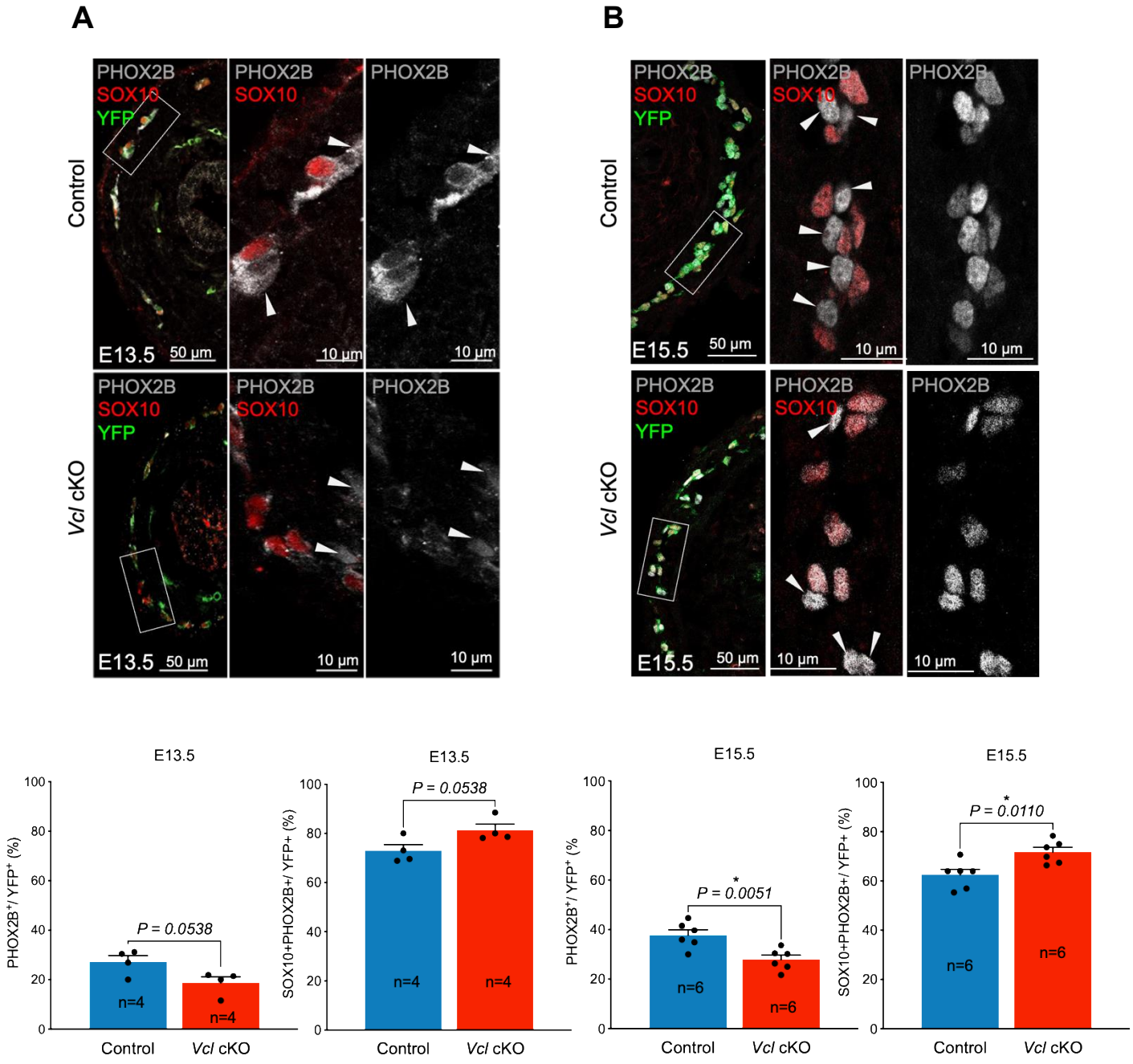

Supplementary Figure 3. Delayed neuronal differentiation of ENCCs in *Vcl* cKO at E13.5 & E15.5. Immunoflurosecence of Phox2b and Sox10 in control (*Wnt1-cre; Rosa26*^{YFP}) and mutant (*Wnt1-cre;Rosa26*^{YFP}*;Vclf/f*) at **(A)** E13.5 and **(B)** E15.5. All ENCCs were labeled with YFP. Bar charts display the quantitative data on the percentages of ENCCs committed to the neuronal lineage (Phox2b+, marked by arrow heads) and the uncommitted (Phox2b^{+}Sox10^{+}) ENCCs. (mean ± SEM, n: number of embryonic guts analyzed, P<0.05 was considered significantly different, student *t*-test, two-sided).

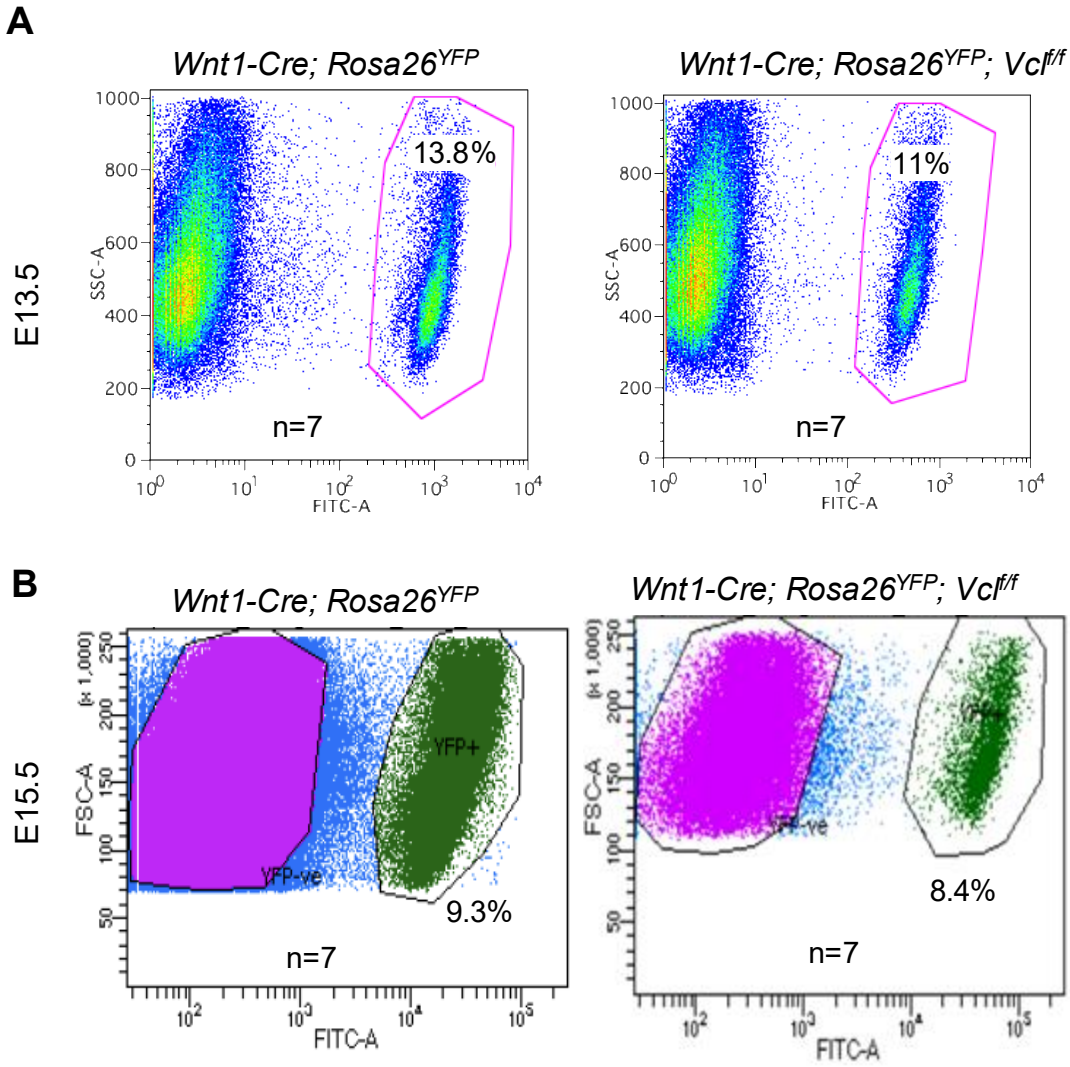

Supplementary Figure 4. Enrichment of ENCCs from the control and *Vcl* cKO guts at E13.5 & E15.5 by FACS. Seven enzyme-dissociated embryonic guts from 2-3 litters were subjected to FACS. The scatter plots show comparable percentages of YFP+ ENCCs were isolated from control and mutant embryonic guts at **(A)** E13.5 and **(B)** E15.5.

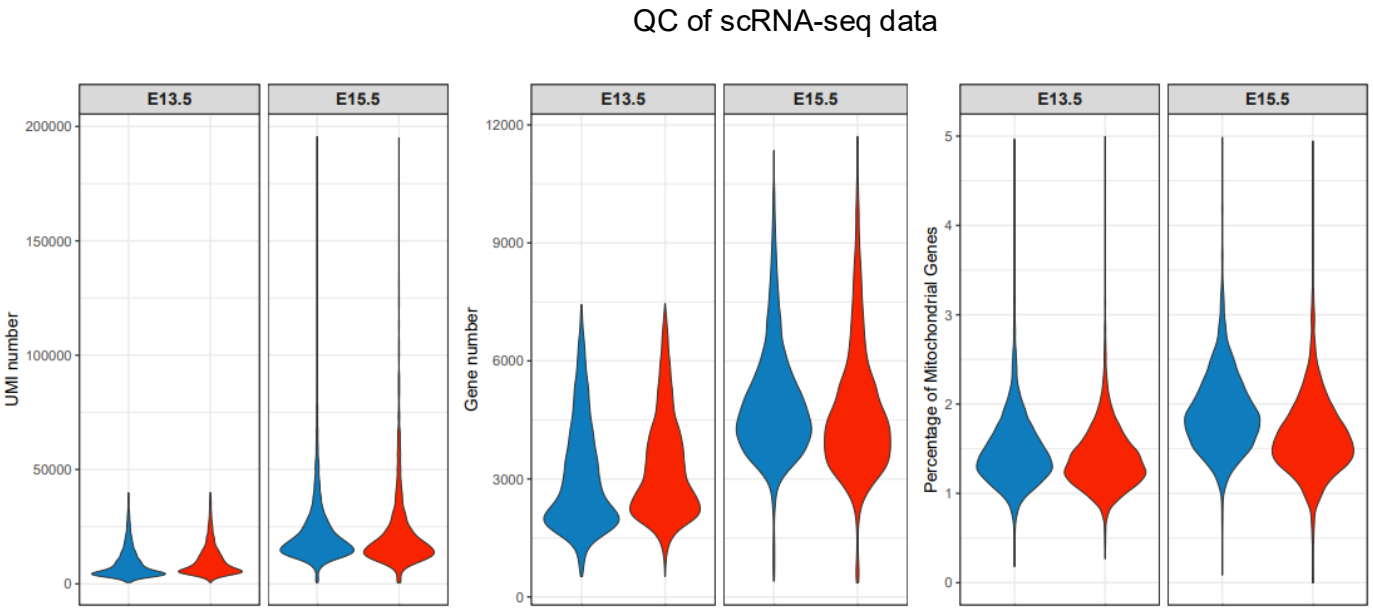

Supplementary Figure 5. Quality control of scRNA-seq data. Violin plots displaying (left) the number of unique molecular identifiers (UMIs) per cell, (middle) the number of detected genes per cell, and (right) the percentage of mitochondrial gene per cell.

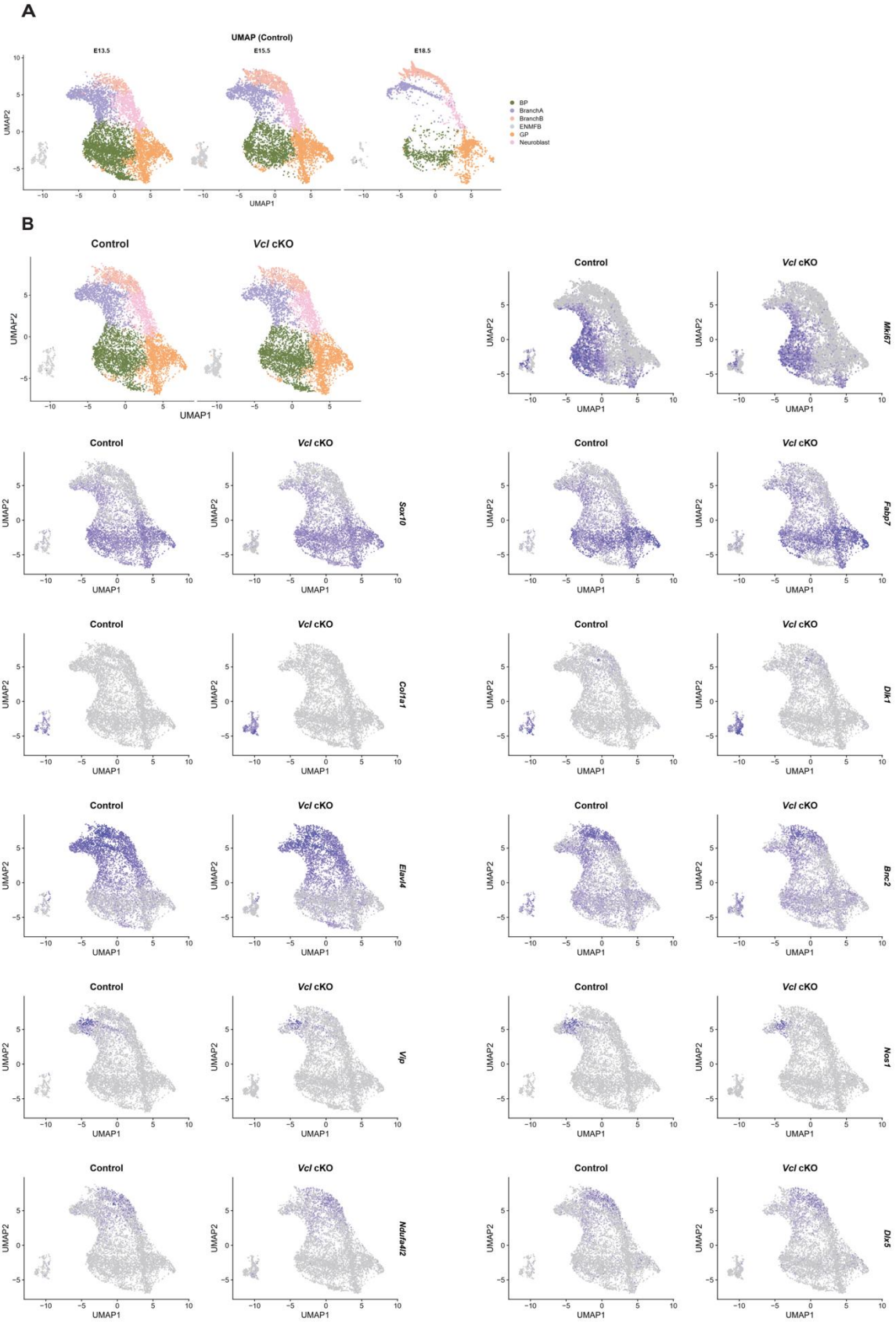

Supplementary Figure 6. Annotation of scRNA-seq data. (A) Integrated UMAP projection of control scRNA-seq data at E13.5, E15.5, and E18.5 from Mikhailova et al. 2021**. (B)** Expression of selected marker genes and proliferative markers in the control and mutants.

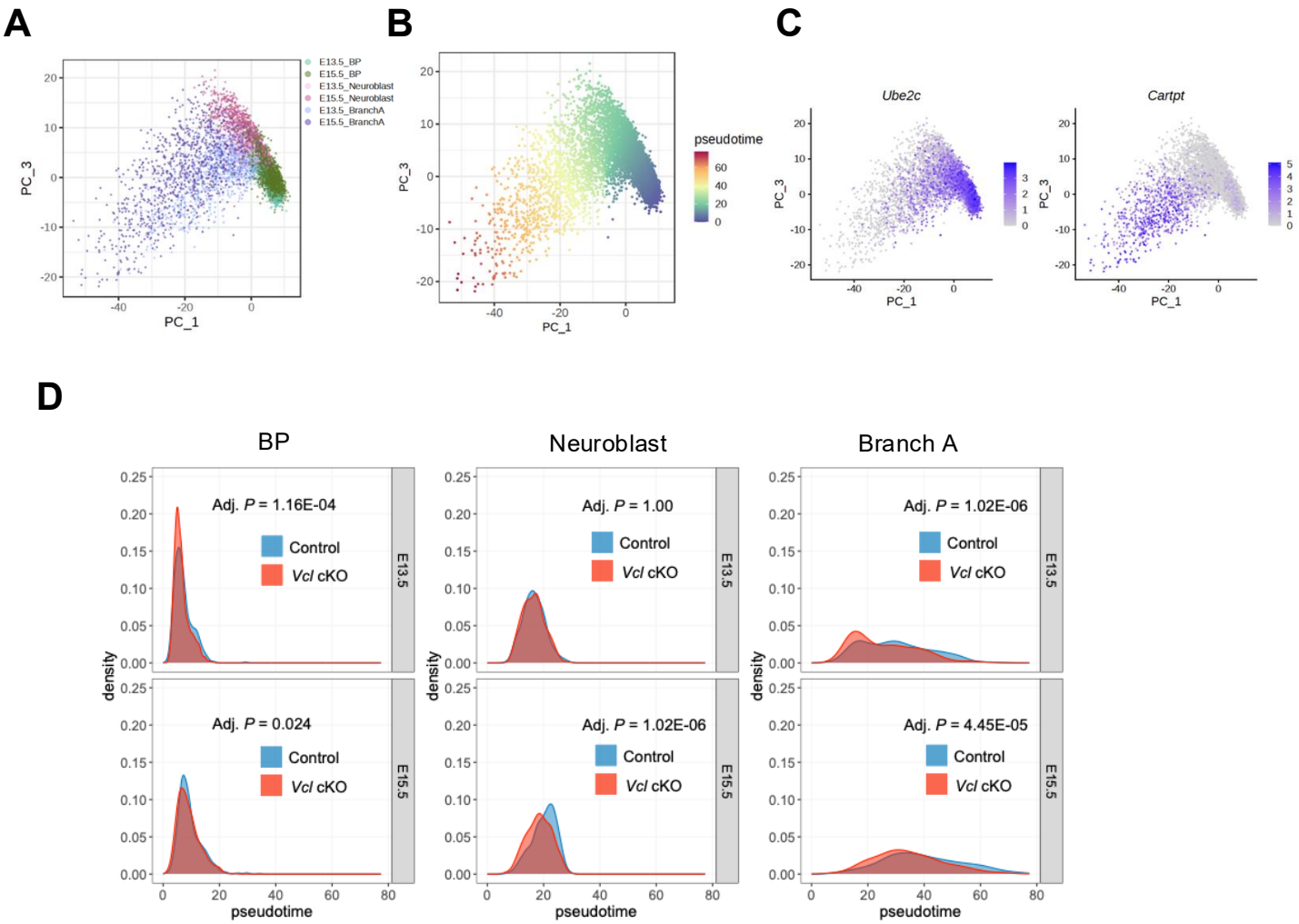

Supplementary Figure 7. Trajectory construction using cells in disrupted cell states. **(A)** Cell distribution in a low-dimensional embedding of PCA1 and PCA3. **(B)** Inferred pseudotime of cells across disrupted cell states. **(C)** Scaled expression of selected marker genes for BP (*Ube2c*) and Branch A neurons (*Cartpt*) in the PCA plot. **(D)** Density plot shows the pseudotime distributions across disrupted cell states. Two-sided asymptotic two-sample Kolmogorov-Smirnov test.

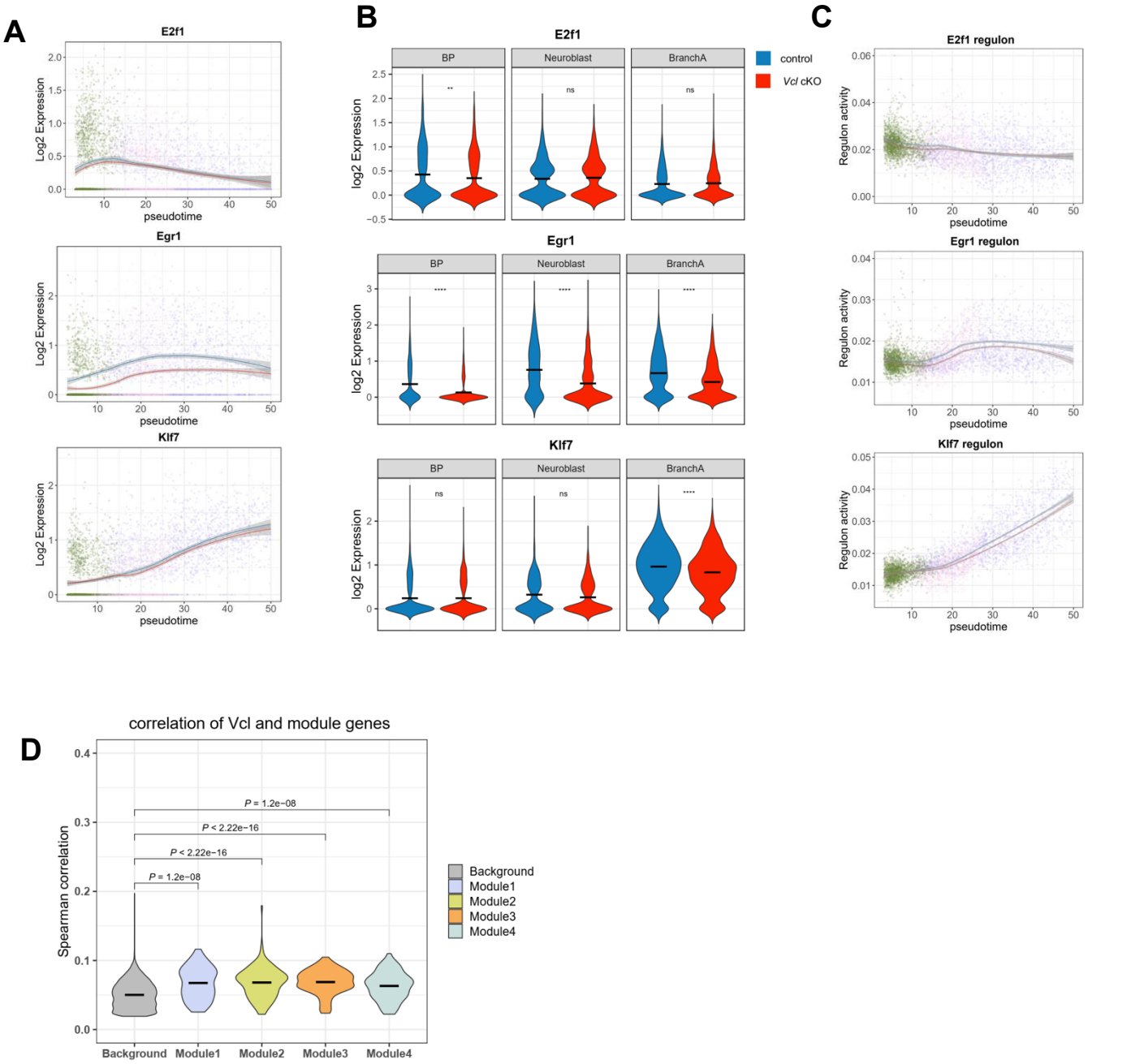

Supplementary Figure 8. Dynamic changes of TFs along trajectory. (A) Expression of TFs along the trajectory. **(B)** Expression of TFs in different cell states. **(C)** Regulon activity along the trajectory. **(D)** Spearman correlation of *Vcl* and genes in modules.

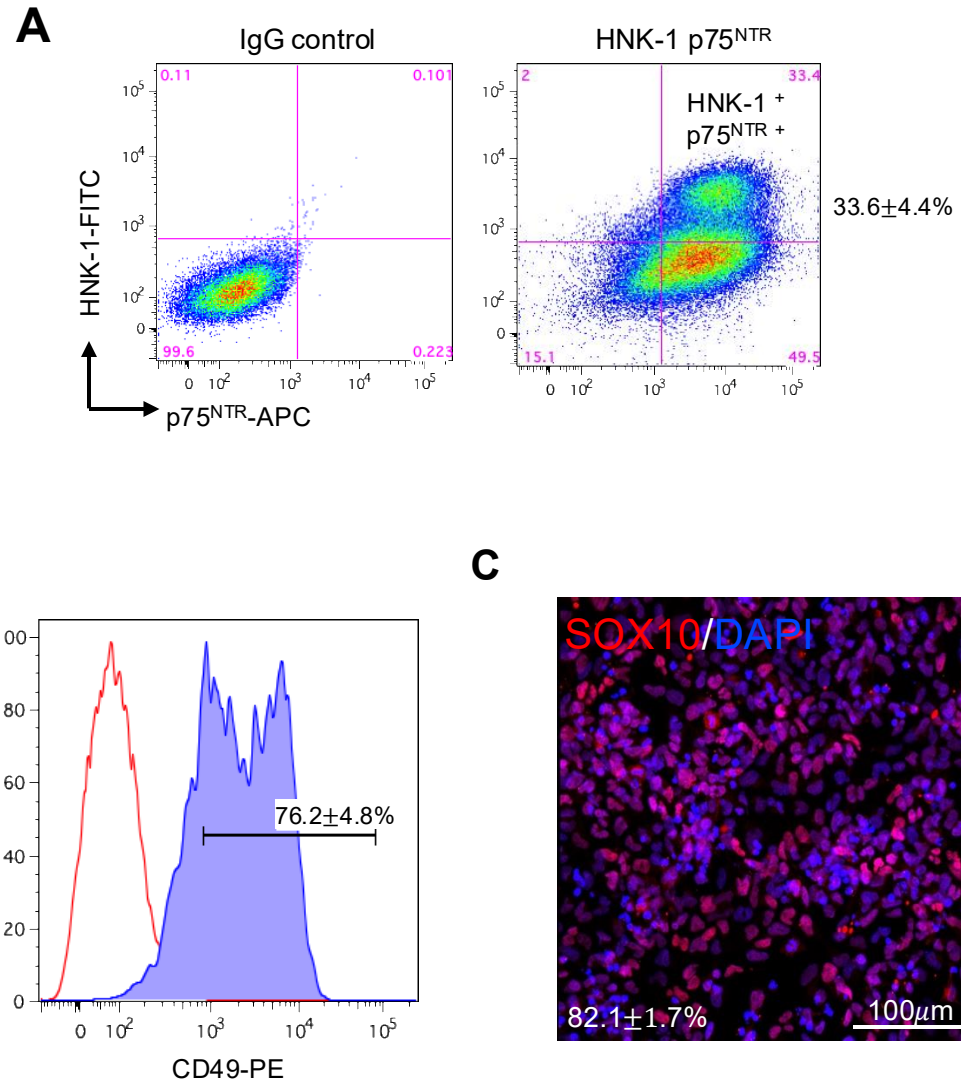

Figure S9. Enrichment and characterization of hiPSC-derived ENCCs. ENCCs were identified and enriched on Days 10 of neural crest induction based on their expression of neural crest markers(HNK-1, p75NTR and CD49) using fluorescent-activated cell sorting (FACS). IgG control was used as a negative control. **(A)** Flow cytometry dot plots show the percentages of cells expressing HNK-1 and p75^{NTR} in each group. HNK-1 and p75^{NTR} double-positive cells were enriched by FACS. **(B**) The majority of HNK-1 and p75^{NTR} double-positive cells (76.2 $\pm$ 4.8%) co-express CD49. **(C)** Immunocytochemistry with antibody against SOX10 is performed in HNK-1 $^{+}$ and p75^{NTR} $^{+}$ cells.

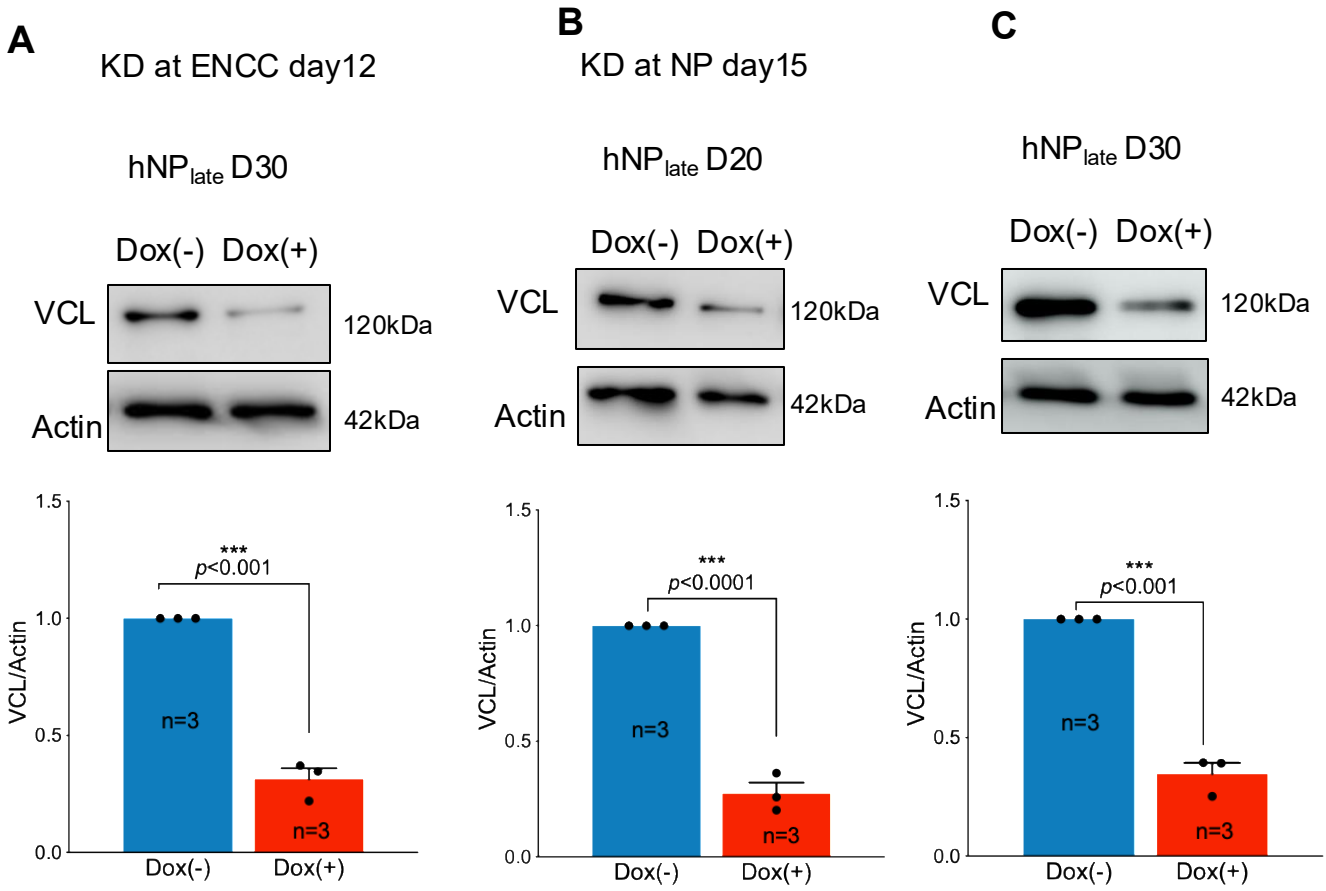

Supplementary Figure 10. Western blots of VCL expression. *VCL* was knocked down in **(A)** ENCCs on Day 12 and **(B & C)** in NP on Day 15. Expression of VCL was detected by Western blotting on Days 20 and 30 of neuronal differentiation, as shown. A representative image from each set is shown. Bar charts illustrate the relative expression of VCL in control and KD cells (mean ± SEM) from three independent experiments. ACTIN was used as the loading control. A *P*-value of <0.05 is considered statistically significant, based on a two-sided Student's *t*-test.

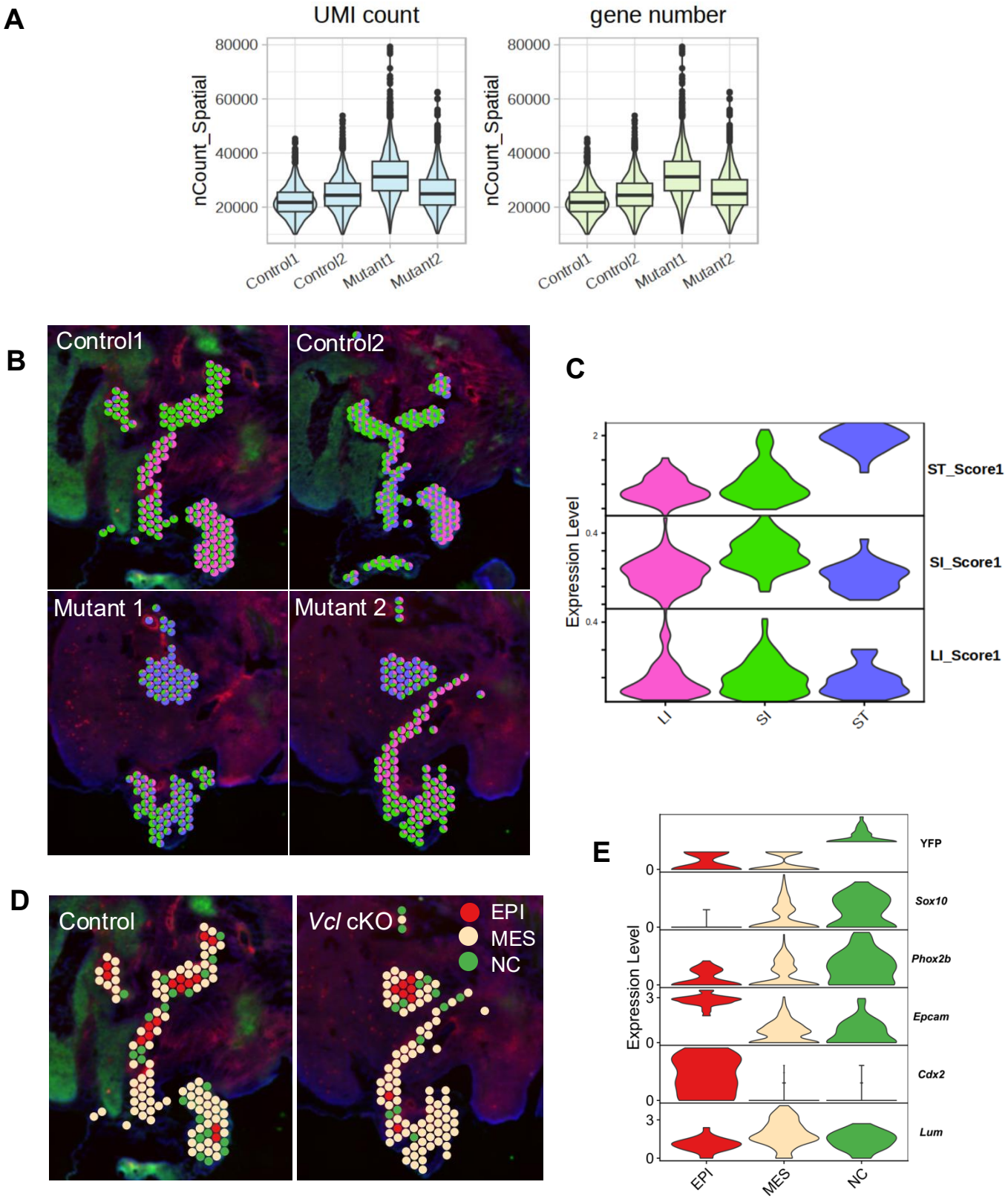

Supplementary Figure 11. Quality control and spatial annotations for gut region at E13.5. (A) The UMI count (nCount_Spatial) and the number of detected gene number (nFeature_Spatial) of 4 datasets of cells from 4 sections of E13.5 control and mutant embryos. **(B)** Spatial scatter pie plot displays inferred region composition in each spot in the gut region. LI, large intestine; SI, small intestine; ST, stomach. **(C)** Violin pot showed the module scores calculated using a set of marker gene of different gut regions. **(D)** Representative images of spatial annotation of all spots using Control 1 and Mutant 2, which comprised comparable numbers of various cell types. Hereafter, they are labeled as Control and *Vcl* cKO, respectively. EPI, epithelium; MES, mesenchymal cells; NC, neural crest cells. **(E)** Violin plot shows the expression of selected marker genes of EPI, MES and NC.

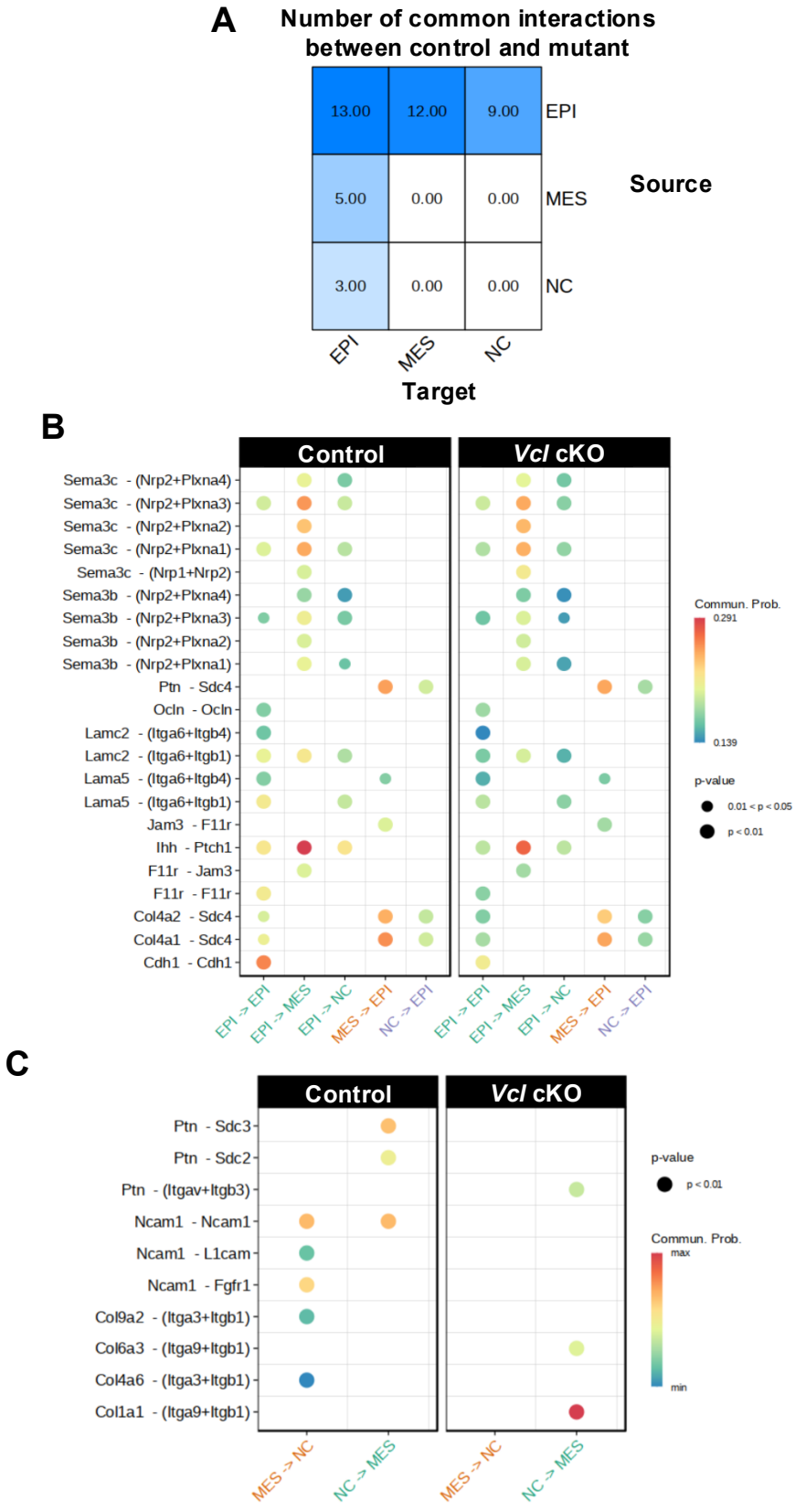

Supplementary Figure 12. Inferred cell-cell interactions in E13.5 Visium data. (A) The heatmap showed the number of common cell-cell interactions occurring between identical cell-type pairs in control and *Vcl* mutant. **(B)** Dot plot shows the common cell-cell interactions in (A). **(C)** The cell-cell interactions in top two signaling pathways of control and mutant, ranked by the total interaction probability as shown in Figure 6C, with only those *P* value < 0.01 displayed.

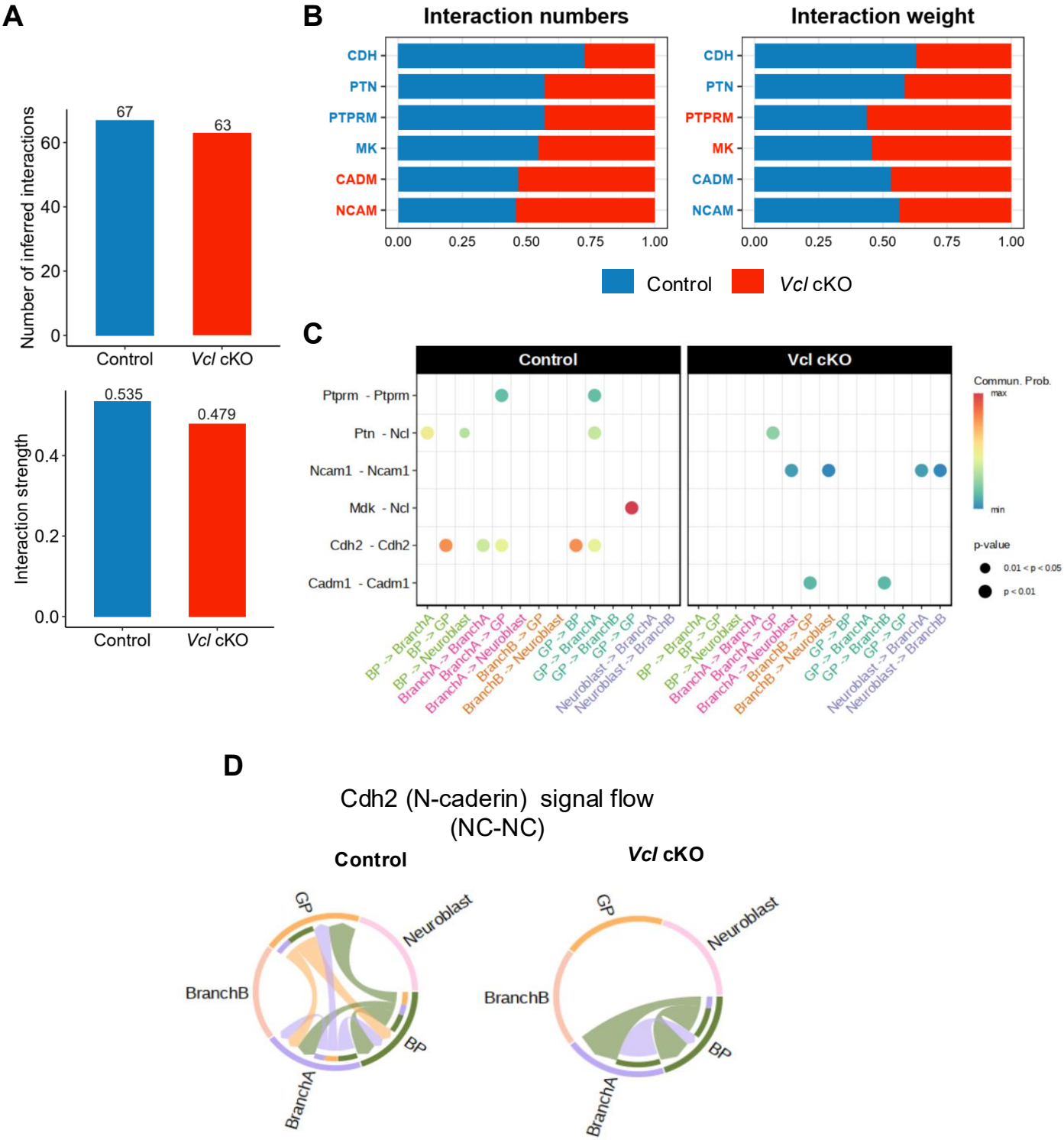

Supplementary Figure 13. Inferred cell-cell interactions using scRNA-seq data at E13.5. **(A)** Total number and strength of cell-cell interactions inferred using E13.5 scRNA-seq data. **(B)** Total number and probability of cell-cell interactions across different signaling pathways. **(C)** The disrupted cell-cell interactions identified as gained or lost in *Vcl* mutant compared to the control. **(D)** Chord diagram shows the signal flow of N-caderin among different cell states.

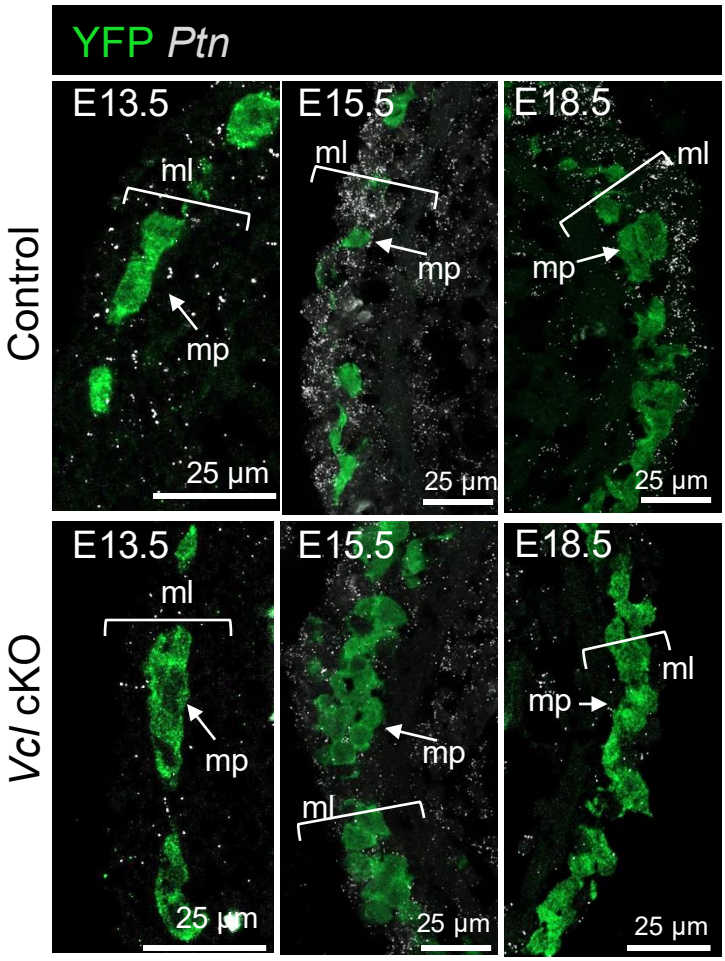

Supplementary Figure 14. Dynamic expression of *Ptn* in ENCCs and gut mesenchyme. RNAscope detected the *Ptn* transcripts in E13.5, E15.5 and E18.5 embryonic guts in control and *Vcl* cKO.

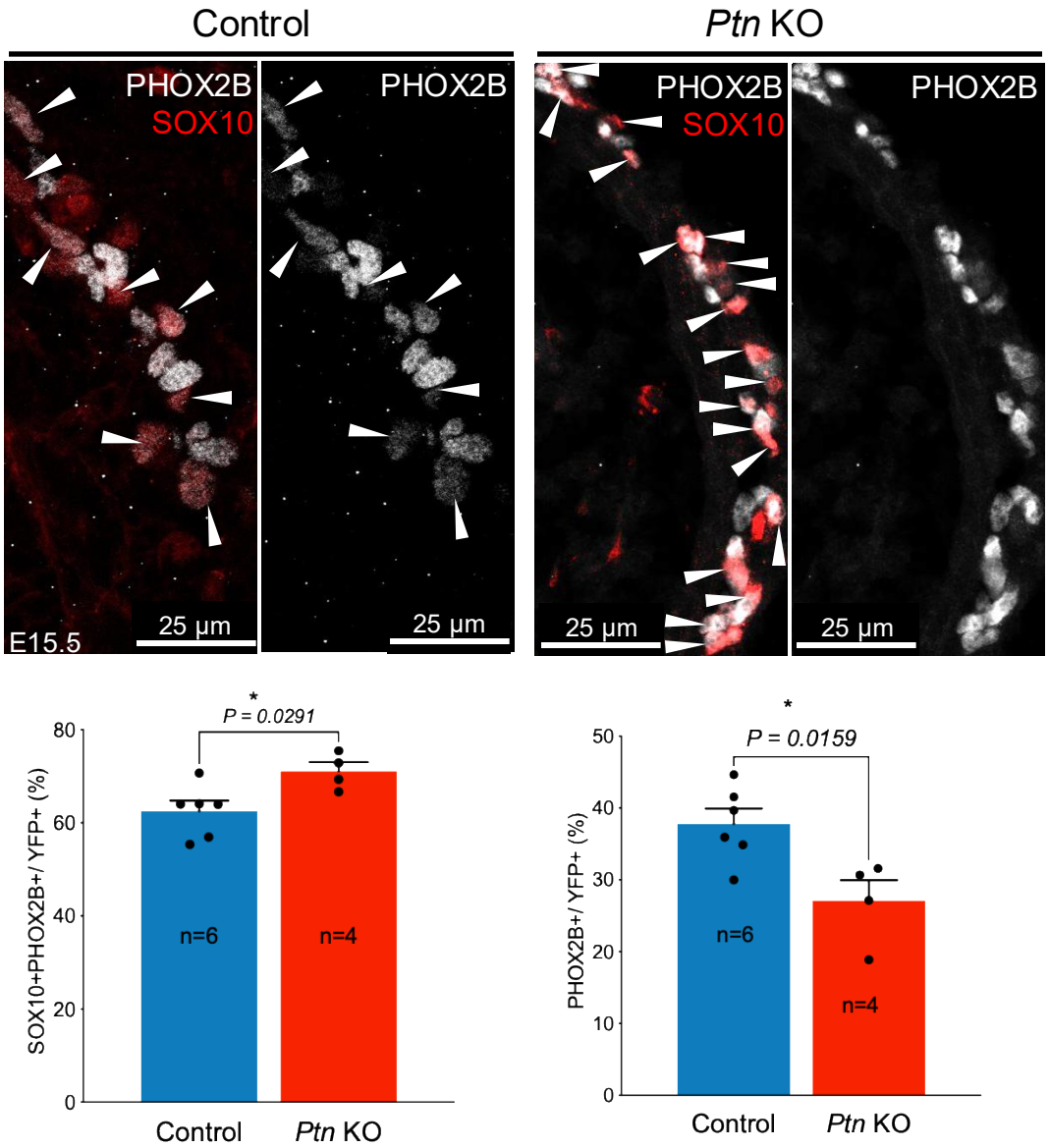

Supplementary Figure 15. Delayed neuronal differentiation of ENCCs in *Ptn* KO at E15.5. Immunoflurosecence of Phox2b and Sox10 in control (*Ptn*$^{+/+}$) and mutant (*Ptn*$^{-/-}$) at E15.5. Bar charts display the quantitative data on the percentages of ENCCs committed to the neuronal lineage (Phox2b+) and the uncommitted (Phox2b^{+}Sox10^{+}, marked by arrow heads) ENCCs. (mean±SEM, n: number of embryonic guts analyzed, P<0.05 was considered significantly different and marked by "*", student *t*-test, two-sided).

Materials and Methods

Patients

We reanalyzed our in-house whole-genome and whole-exome sequencing datasets(1-3) to identify potential mutation(s) affecting *VCL*. A total of 94 sporadic (no family history) HSCR patients with short-segment aganglionosis were included in this study. These patients are Chinese and were consecutively recruited at Queen Mary Hospital, where they underwent surgery. Seventy-two patients were male and twenty-two were female. Twelve patients (three females and nine males) had associated anomalies in the heart, including ductus arteriosus (PDA), atrioventricular septal defect, and bicuspid aortic stenosis. Another twelve male and seven female patients had other defined syndromes such as Down syndrome, Ondine's Curse, and Wolff-Parkinson-White (WPS) syndrome. The remaining patients had no associated anomalies (isolated HSCR). HSCR diagnosis was based on histological examination of either biopsy or surgical resection material for the absence of enteric plexuses. Informed consent was obtained from all participants and the study was approved by the institutional review board of the University of Hong Kong and the Hospital Authority ((HKU/HA HKW IRB) UW 13-225).

We used one program which integrates all predictions made by other programs: Variant pathogenecity was assessed by an in-house program KGGSeq(4). KGGSeq is a software platform that consists of bioinformatics and statistical genetics functions, making use of valuable biological resources and knowledge, providing a comprehensive and efficient framework to filter and prioritize genetic variants from whole-exome and whole-genome sequencing data. Importantly, KGGSeq integrates “knowledge” resources from epigenetic databases, biological pathways and protein-protein interaction networks to annotate the genes that harbour any post-QC variants as well as to predict the potential pathogenicity of their variants. For the later, KGGSeq integrates 4 prediction programs (Polyphen2, Sift, MutationTaster and Likelihood ratio) which are weighted by logistic regression.

Those rare variants predicted deleterious, unique to the patients analyzed and whose MAF was zero or <1% in public databases (The 1000 Genome Project, the NIH Exome Sequence Project of 6500 individuals -ESP6500-) or in-house exome sequencing projects (N=900 Chinese individuals) were selected for validation. Thus, Sanger sequencing of the patients' DNA was performed to validate the next-generation sequencing data. Sanger sequencing of parental DNA was also performed (when available) to assess the origin of the variant.

Construct construction

The full-length, head, and tail domains of human *VCL* (NM 00373) were obtained by PCR with specific primers (Supplementary Table 1) and subcloned into pCMV-GFP (Addgene, Plasmid #11153), pFLAG-CMV2 expression vector (Sigma), and pCMV-Myc-N (Clonetech), respectively. HSCR-associated mutations were then introduced into VCL expression constructs using the QuikChange Lightning Site-Directed Mutagenesis Kit (Agilent Technologies, Santa Clara, CA) with specific primers listed in Supplementary Table 1 according to the manufacturer's protocol. DNA sequence and mutations were confirmed by Sanger sequencing. The wild-type and mutated *VCL* expression constructs were subsequently transfected into HeLa cells, the human cervical cancer cells (with expression of MYC-C), and subjected to immunofluorescent and pull-down assays.

Mice

Wnt1-Cre (strain# 022137), *Rosa26*^{YFP} (strain# 006148) and *Vcl*$^{f/f}$ (strain# 028451) mice were purchased from Jackson Lab. *Ptn* heterozygous knockout (T028403) mice were purchased from GemPharmatech. Mice were maintained in a mix outbred background of C57. Embryos were collected at different embryonic days dated from the day of the vaginal plug (E0.5). For each experiment, a representative result and the corresponding mean value ± SEM were

presented from at least five analyzed embryos. The number of individual embryos analyzed (n) is shown in all charts. Source data are provided as a Source Data file. Primers for genotyping are listed in Supplementary Table 2. Animals were kept in the Animal Laboratory of the University of Hong Kong, and all experiments were performed in accordance with procedures approved by the committee on the Use of Live Animals, the University of Hong Kong (CULATR 23-493 and CULATR 23-029). Our study examined male and female animals, and similar findings are reported for both sexes.

Generation of an inducible Cas9 human induced pluripotent stem cells (iCas9-hiPSCs)

A control hiPSC cell line (UE02302) was kindly provided by Dr. Guangjin Pan (Guangzhou Institutes of Biomedicine and Health, Chinese Academy of Sciences, China)(5). hiPSCs used in this study were at the intermediate (35-65) passage numbers and maintained on Matrigel (Corning, 354277)-coated plate with mTeSR1 medium (StemCell Technologies, 85850). To generate a hiPCS line with an inducible expression of Cas9, we adopted the doxycycline inducible Cas9 system published by Gonzalez *et al*(6). The inducible cassettes, one containing the iCas9 coding sequence under the regulation of the tight TRE promoter and the other carrying the M2rtTA tetracycline response element(7), were obtained from Addgene (access number #58409 and #60843). These two cassettes were sequentially targeted into the AAVS1 loci by CRISPR-Cas9D10a nickase-mediated homologous recombination with two gRNAs (Supplementary Table 1). It was followed by selection with puromycin and neomycin, and the properly targeted neomycin and puromycin resistant clones were selected using PCR. The inducible expression of Cas9 was validated by Western blot.

Derivation of enteric neural crest (ENCC) from iCas9- iPSC lines

At day 0, iCas9-hiPSCs were seeded on Matrigel-coated plate (10^5 cells cm^{-2}) in iPS cell medium containing 10 ng ml^{-1} FGF2 and 10 μM Y-27632 (Tocris Bioscience, 1254). Differentiation was then initiated by replacing iPSC medium with KSR medium, containing KnockOut DMEM (Thermo Fisher Scientific, 10829018) plus 15% KSR, 1% NEAA, 1% L-glutamine, 1X β-mercaptoethanol, 1% penicillin-streptomycin, LDN193189 (100 nM, Reprocell, 04-0074) and SB431542 (10 μM, Abcam, ab120163). The dual SMAD inhibitors and a potent GSK inhibitor were added at different time frame during the NC induction, including LDN193189 (from day 0 to day 3), SB431542 (from day 0 to day 4), 3 μM CHIR99021 (from day 2 to day 10, Reprocell, 04-0004). The NC cells were finally caudalized with 1 μM retinoic acid (Abcam, ab120728) (from day 6 to day 9). The KSR medium was gradually changed to N2 medium at day 4 by increasing N2 from 25% to 75% from day 4 to 9[8]. The N2 medium contained neural basal medium (Thermo Fisher Scientific, 22103049) and DMEM/F12 in 1:1 ratio supplemented with 0.5% N2 supplement (Thermo Fisher Scientific, 17502048), 1% B27 supplement (Thermo Fisher Scientific, 17504044), 5 μg ml^{-1} insulin (Thermo Fisher Scientific, 12585014) and 1% penicillin-streptomycin. The ENCCs were enriched by FACS with antibodies against $p75^{NTR}$ and HNK-1 at day 10 of the differentiation as described(8, 9).

In vitro differentiation of ENCCs to neuronal progenitors (NPs)

Around 40 thousand FACS-enriched ENCCs were seeded as droplets on poly-ornithine/laminin/fibronectin (PO/LM/FN)-coated 24 well plate in N2 medium containing 10ng ml^{-1} FGF2, 3 μM CHIR99021 and 10 μM Y-27632. The neuronal differentiation started 48 hours later and the attached ENCCs were then cultured with N2 medium containing BDNF (10ng ml^{-1} Peprotech, 450-01), GDNF (10 ng ml^{-1}, Peprotech, 450-10) and ascorbic acid (200

μM, Sigma, A4034-100G), NT-3 (10ng ml^{-1}, Peprotech, 450-03), NGF (10ng ml^{-1}, PeproTech, 450-01) and cAMP (1 μM, Sigma, D0260).

Fluorescence activated cell sorting (FACS)

The 10 day-differentiated cells were dissociated with Accutase and then incubated with antibodies against neural crest markers including APC-HNK-1, FITC-$p75^{NTR}$ and ITGA4-PE for 30-45 minutes on ice. The stained cells were washed and resuspended in PBS with 2% FBS. The HNK-1 and $p75^{NTR}$ double-positive cells were enriched with BD FACSAria III Cell Sorter (Becton Dickinson Immunocytometry Systems, San Jose, CA, USA). The HNK-1 and $p75^{NTR}$ double-positive cells were gated and sorted using the four-way purity mode and the purity of sorted cells was >96% and evaluated by flow cytometry. The sorted neural crest cells were collected for immunostaining or subsequent experiments. A list of primary antibodies and the working dilutions is provided in Supplementary Table 1. Isotype-matched antibodies were used as controls. FlowJo version 8.2 (Tree Star, Inc.)

Doxycycline-induced Cas9-mediated cleavage of VCL in ENCCs

Expression of Cas9 was induced on day 10, right after the FACS-enrichment or day 13 by addition of 2 μg ml^{-1} doxycycline (DOX), and the ENCCs were then transfected with sgRNA on day 12 or 15. On the day of transfection, the medium was replaced with neuronal differentiation medium without antibiotics. Predesigned Alt-R™ CRISPR-Cas9 sgRNAs targeting exon 1 (Hs.Cas9.VCL.1.AB) and exon 3 (Hs.Cas9.VCL.1.AA) of human *VCL* gene (Supplementary Table 1) were purchased from Integrated DNA Technologies (IDT, Coralville, USA). The sgRNAs were diluted in Opti-MEM and then mixed with Lipofectamine™ RNAiMAX (Invitrogen, USA) according to the manufacturer's protocol. The final concentration of each sgRNA used for transfection was 10 nM. The transfected cells were

collected at day 20 and day 30 during the neuronal lineage differentiation for immunofluorescence staining and Western blotting analyses.

Co-IP

co-IP was performed as previously described(10). Briefly, the human cells were lysed in 50 mM Tris-HCl, pH7.5, 100 mM NaCl, 1% Triton X-100, 0.1 mM EDTA, 0.5 mM $MgCl_2$, 10% glycerol, protease inhibitor cocktail (Roche), phosphatase inhibitor cocktail (Roche), and 10 μM pervanadate (NEB). Lysates were incubated with anti-GFP or anti-FLAG M2 Magnetic Beads (Sigma, M8823) overnight at 4 °C. Antibody/protein complexes were washed with lysis buffer for four times and analyzed by Western Blotting.

Immunoblots

hiPSC-derived ENCCs or embryonic guts were collected and then lysed with cell lysis buffer containing 20 mM Tris (pH 7.5), 150 mM NaCl, 1 mM EDTA, 1 mM EGTA, 1% Triton X-100, 2.5 mM sodium pyrophosphate, 1 mM β-glycerophosphate, 1 mM Na_3VO_4, 1 μg/mL leupeptin and 1 mM phenylmethanesulfonyl fluoride (PMSF). Cell lysates containing 5-25 μg of total protein were separated on 8-12% SDS-polyacrylamide gels and blotted onto nitrocellulose membranes. The membranes were then incubated with primary antibodies (Supplementary Table 3). The same membranes were probed with a 1:5000 dilution of anti-actin monoclonal or anti-Gapdh antibody to ensure equal loading of cell protein per lane. All blots were incubated with 1:5000 dilutions of secondary horseradish peroxidase-conjugated anti-mouse or anti-rabbit antibody (Supplementary Table 4). Antibody-bound proteins were visualized using a chemiluminescence system (Amersham Pharmacia Biotech). The representative pictures of at least 3 independent assays were shown.

Acetylcholinesterase (AChE) stain

Embryonic guts at E18.5 were first dissected in PBS and fixed in 4% PFA for 2-4 hours at 4ºC. The Acetylcholinesterase Rapid Staining Kit (MBL #8450) was used to stain the ENS following the manufacturer's protocol. The whole-mount images were captured using Leica MZ10F stereomicroscope.

Immunofluorescence studies

Immunocytochemistry

Immunocytochemistry - Cells were fixed with 4% PFA in PBS at room temperature for 30 min, followed by blocking with 1% bovine serum albumin (BSA) (Thermo Scientific, 23209) with 0.1% Triton X-100 (Sigma, T8787) in PBS. Cells were then incubated in primary antibody overnight at 4°C, followed by host-appropriate Alexa Fluor -488 or 594 secondary antibody (Molecular Probes, Invitrogen) (Tables S3 & 4) for 1 h at room temperature. Cells were then counterstained with 1:2000 DAPI (Thermo Fisher Scientific, 62248) in PBS for 10 min at room temperature to detect nuclei and mounted with ProLong Diamond Antifade Mountant with DAPI (Thermo Fisher Scientific, P36971). All the fluorescence images were acquired by Carl Zeiss LSM800 or LSM900 confocal microscope. Quantitative image analysis of differentiated cells was performed with ImageJ plug-in tool. The total signal of the specific marker was normalized with DAPI signal and the values reported in bar charts represent the mean ± SEM.

Whole mount immunohistochemistry - Embryonic guts were first dissected in PBS, fixed in 4% PFA for 2-4 hours at 4ºC. The dissected guts were then washed with 1% PBST for 30 minutes at RT for 3 times and incubated in blocking buffer (1% PBST with 10% FBS and 0.2% sodium azide) for 2 hours at RT. Subsequently, they were incubated with primary antibodies (diluted in PBS with 20% DMSO and 5% donkey serum) at 4ºC for 2-3 days. The guts were

washed with 1% PBST for 10 minutes for 3 times and incubated with secondary antibody for 2-3 days at RT. After washing with 1% PBST for 10 minutes for 3 times. The guts were dehydrated in 24-well dishes in graded methanol/ PBS (approximately 500 mL/well, extra if needed to cover, 30 minutes/wash: 50% methanol, 70% methanol, 80% methanol, 95% methanol, 100% methanol x3, room temperature, on rocker). The rehydrated guts were then incubated in Murray's Clear (2:1 benzyl benzoate: benzyl alcohol) until completely translucent (15–30 minutes, room temperature). Guts were then mounted on glass slides in Murray's Clear and imaged within 48 hours as described previously[11]. Whole mount immunofluorescence images were captured using Carl Zeiss LSM 800 or LSM900 confocal microscope.

Immunohistochemistry - For section immunohistochemistry, embryos were fixed in 4% paraformaldehyde (PFA) in PBS at 4ºC, dehydrated and cryoprotected in 30% sucrose in PBS at 4ºC and embedded in OCT compound (Tissue-Tek). The sections were blocked in PBS containing 10% normal goat or horse serum (DAKO) for 1 hour at room temperature, then incubated overnight at 4ºC in a mixture of the primary antibodies (Supplementary Table 3). After washing, the immunosignals were then detected using the secondary antibody conjugated with Alexa Fluor 488 or 594 (Supplementary Table 4). Tissue sections were photographed using a Carl Zeiss LSM 800 or LSM900 confocal microscope.

Confocal microscopy and live imaging - while section immunofluorescence images were captured using. Carl Zeiss LSM 800 was also used for live imaging where Z-stack images were captured every 5 minutes for 12-15 hours. Live imaging was performed on E12.5 guts using the conditions described previously(11, 12). Immunofluorescence images were processed and analysed using ImageJ (NIH). For live imaging of ENCC migration, ENCCs were tracked by Manual Tracking plugin and the tracks generated were analysed using Chemotaxis and

Migration Tool plugin (ibidi) to calculate cell speed, net speed and persistence. Persistence of ENCC migration was calculated as the ratio of net distance travelled by ENCC to the total distance travelled by ENCC.

Focal adhesion size analysis

Images were processed using ImageJ version 2.16. For calculating focal adhesion size, cells were stained with Paxillin or VCL. The captured FITC or Texas-Red images were background-subtracted, and a threshold was set to restrict analysis to FA. The images were then converted to binary mode, and the FA size (area) per cell was measured using ImageJ plug-in software. The average FA size of 60 cells from three independent assays is shown in the bar chart (mean ± SEM).

Droplet-based single-cell RNA-sequencing (scRNA-seq)

The FACS-sorted cells were then subjected to droplet-based scRNA-seq using Chromium Single Cell platform and Single Cell 3' Library Kits (10x Genomics) in Centre of PanorOmic Science (CPOS), The University of Hong Kong. In brief, cells were encapsulated into Gel Beads-in-emulsion (GEMs) by the 10X Chromium Single Cell Controller, followed by reverse transcription and library preparation to become a pool of cDNA libraries. Libraries were then purified and sequenced on an Illumina™ NextSeq 500 according to the manufacturer's protocol.

Processing and quality control of single-cell RNA sequencing data - To address potential variations introduced by different software versions, we reprocessed our previously published scRNA-seq data of YFP-labelled ENCCs at E13.5(11). FASTQ files of control and *Vcl* mutant samples at E13.5 and E15.5 were processed and aligned to the mm10 mouse reference

transcriptome (mm10-2020-A-2.0.0) to generate gene-by-cell matrices, using the 10x Genomics Cellranger software (v7.2.0) with default parameters. The gene-by-cell matrices were loaded in the Seurat(13) package for the quality control. To mitigate the doublet, we filtered the cells on nCount_RNA metrics. For E13.5 samples, cells were filtered based on the criteria "500 < nFeature_RNA & nFeature_RNA < 7500 & percent.mt < 5 & nCount_RNA < 40000". For E15.5 samples, cells were retained if "percent.mt < 5 & nCount_RNA < 2e+05 & nFeature_RNA > 200". Finally, we got 30,157 cells as shown in Supplementary Data 2.

Single-cell RNA-seq data integration and annotation - Control data at E13.5 and E15.5 were integrated for main cell type annotation. Expression matrices were normalized using the "LogNormalize" method in Seurat. After scaling the data, principal component analysis (PCA) was performed using the "RunPCA" function on the top 2,000 variable genes for each of the four sample datasets separately. The control data from both stages were then integrated using the anchor-based reciprocal PCA integration method implemented in the Seurat R package. Cells were finally annotated as bipotent progenitors (BP), glial progenitors (GP), neurons, and enteric mesothelial fibroblasts (ENMFB) based on the expression of canonical marker genes and proliferative markers as shown in Figure 5C. Using annotations in control data as a reference, *Vcl* mutant data were annotated via the label transfer method in Seurat and based on the clustering results.

To identify the branching neuronal lineage, data in this study were integrated with the scRNA-seq data of the enteric nervous system of the small intestine at E18.5(14). The E18.5 data were reprocessed and annotated as GP, BP, Neuroblast, Branch A and Branch B neurons based on the canonical marker gene expression and branch-specific transcriptional factors identified in the original study(14). After integrating the data from all three stages using RPCA anchor-

based method, the neuron cells at E13.5 and E15.5 were categorized as Neuroblast, Branch A or Branch B based on the label transfer results and clustering results in the integrated UMAP embedding. Marker genes for each cell type were identified for validation, using the "FindAllMarkers" function in Seurat, with the parameter "min.pct" set to 0.25. The marker information is shown in Supplementary Data 3.

Proportion analysis

Due to sample size constraints, the direct statistical testing on the comparison of cell type proportion was not feasible. To address this, we employed scanpro(15) (a tool designed for proportion analysis in single-cell sequencing data) to perform the proportion analysis for statistical evaluation. In our case, scanpro generated pseudo-replicates on each sample and used them for the following Student's *t*-test with the transform model setting as "arcsin".

RNA velocity analysis - The RNA velocity is inferred independently for the control and *Vcl* mutant datasets at E13.5 and E15.5 data using velocyto v0.17 (http://velocyto.org/velocyto.py/index.html), The results were subsequently integrated for comprehensive velocity visualisation using scVelo(16).

Pseudotime inference - To remove the cell number effect, we standardized the total number of cells (3404) in disrupted cell states in control and mutant groups for the pseudotime inference. As the distribution of cells in principal components 1 (PC1) and 3 (PC3) reflected a continuous pseudotemporal trajectory from BP-Branch A lineage, the pseudotime was inferred using SlingShot(17) based on these two dimensions. In this analysis, BP is designated as the starting cluster, with Branch A as the terminal cluster.

Differential expression analysis and pathway enrichment analysis - Monocle v2.30.1(18) was used to identify the differentially expressed genes between control and mutant in the corresponding cell states. Genes with FDR-adjusted *P* value less than 0.05 were considered significant and used in downstream analysis. UP and down-regulated genes are determined by the mean raw count of each gene in the control and mutant cells. Gene ontology (GO) term enrichment analyses and Kyoto Encyclopedia of Genes and Genomes (KEGG) enrichment analyses were performed using clusterProfiler(19) R package. Terms that had an adjusted *P* value < 0.01 were defined as significantly enriched.

Gene regulatory network inference - The DEGs of E13.5 BP, E15.5 Neuroblast, E13.5 Branch A and E15.5 Branch A were used for GO enrichment analysis. Among the top 50 pathways ranked by the number of DEGs, the 10 most disrupted pathways in each cell state were identified by the log2 fold changes of the pathway scores between control and *Vcl* mutants. These scores were calculated using all the genes involved in the pathways by AUCell(20). Next, we grouped the DEGs from the 10 most disrupted pathways in each cell state using the gene regulatory network inference strategy implemented in SCENIC[19] R package. This analysis utilized the mouse TFs reference from CisTarget (https://resources.aertslab.org/cistarget/) and the motif scores within the 10 kb flanking regions of the TSS of the genes (https://resources.aertslab.org/cistarget/databases/mus_musculus/mm10/refseq_r80/mc9nr/gene_based/). Of 640 DEGs, 447 genes were identified as the target genes of *E2f1*, *Egr1*, and *Klf7*. Then, these target genes were categorized as four modules based on the regulatory relationship. Based on TF expression and regulon activity along the pseudotemporal trajectory, the modules were assigned to their corresponding cell states. GO enrichment was performed on the genes within modules, where the top 2 pathways ranked by the gene count were

presented. To assess the directionality of changes in the associated biological processes, module scores were calculated using the AUCell(20).

Protein-protein interaction (PPI) network analysis - The genes in modules and *Vcl* were uploaded to STRING database for the PPI inference. To ensure reliable interactions, we exclusively included PPIs derived from curated databases and experimental evidence, and integrated them into the gene regulatory network. Specifically, we selected only "Experiments" and "Databases" as active interaction sources on the STRING website, with the medium confidence score set to the default value of 0.4 in the "minimum required interaction score" section of the settings.

Spearman correlation - Spearman correlations were calculated using the “corr.test” function in R. Only the gene pairs with P value < 0.05 were kept. Genes detected but not included in the modules were designated as the background group. The comparisons of correlations used two-sided Wilcoxon test.

Spatial transcriptomic analysis

Spatial transcriptomics was carried out using the 10x Genomics Visium platform with Visium Spatial Gene Expression Slides & Reagent kits (PN-1000187). 16 μm sagittal sections from OCT-embedded fresh frozen control (*Wnt1-Cre*, $Rosa26^{YFP}$) and mutant (*Wnt1-Cre*, $Rosa26^{YFP};Vcl^{f/f}$) embryos at E13.5 were mounted onto the Visium Spatial slides. The innate YFP signals on the fresh-frozen sections were captured using Nikon Ti2-E Widefield Microscope for the subsequent identification of NCC derivatives in the sections. The sections were then fixed with ice-cold methanol for 20 min and counterstained with DAPI and Alexa Fluor 594 Phalloidin (Thermo Fisher Scientific, A12381) to detect nuclei. The images were

captured using the same Nikon Ti2-E Widefield fluorescent microscope and different fluorescence channels were aligned using Carl Zeiss ZEN lite software. The stained sections were then permeabilized for 12 min to release mRNAs, which bind to the spatially barcoded-oligos present in the underlying spots and reverse transcribed, according to the manufacturer's protocol. Libraries prepared from the cDNAs were sequenced on the Illumina™ NovaSeq 6000 at >50,000 reads per spot generating >400M reads per section. Spaceranger software (version 3.1.0, 10x Genomics) was used to align and obtain raw counts from each of the spots on the Visium spatial transcriptomics slides against the GRCm39 mouse genome reference data.

Processing of the spatial transcriptomic data - Sequencing read alignment, fiducial/tissue detection, and spot barcode/UMI counting of the spatial transcriptomic data were performed using the 10x Genomics toolkit Space Ranger (v2.0.1) with a modified reference genome (mm10-2020-A) with YFP gene contig added. Downstream analysis was conducted using Seurat. Quality control included removal of spots with fewer than 10K unique molecular identifiers (UMI) or fewer than 4K expressed genes.

Cell type assignment in spatial transcriptome data - Initially, the gut regions were manually selected based on the histological images using Loupe Browser 8 from 10x Genomics (https://www.10xgenomics.com/cn/products/loupe-browser). These regions were then further defined based on the expression of marker genes of gut regions. For the large intestine, small intestine, and stomach regions, spots were assigned based on the deconvolution results of CARD(21) using the corresponding scRNA-seq dataset of embryonic guts from the published dataset(22). Employing a similar strategy, the spots were further annotated as epithelial (EPI), mesenchymal cells (MES), and neural crest cells (NC). Specifically, the spots with scaled *YFP* expression higher than 1 were annotated as NC cells.

Cell-cell interactions inference - The cell-cell interactions were inferred using Cellchat v1.61(23). Specifically, we focused on the DEGs when inferring the cell-cell interactions on scRNA-seq data. Interactions that included at least one DEG in both the ligand and receptor were retained. Those with a *P* value < 0.05 were considered significant. The loss and gain interactions in *Vcl* mutant were finally visualized using dot plot. In the spatial transcriptome data, we focused on the large intestine regions that share similar spatial locations, because the most pronounced aberrant phenotype was observed in the colon of mice. Few EPI were identified in the large intestine; thus, the EPI in other regions were also included in the communication inference. Given that disrupted interactions predominantly involve NC and EPI, and the *Vcl* deletion is effective only in NC, our analysis concentrated on interactions within NC and other cell types.

The Major Resources Tables are provided as the Supplemental Material.

References:

1. Gui H, et al. Whole exome sequencing coupled with unbiased functional analysis reveals new Hirschsprung disease genes. *Genome Biol.* 2017;18(1):48.
2. Tang CS, et al. Identification of Genes Associated With Hirschsprung Disease, Based on Whole-Genome Sequence Analysis, and Potential Effects on Enteric Nervous System Development. *Gastroenterology.* 2018;155(6):1908-22 e5.
3. Tang CS, et al. Uncovering the genetic lesions underlying the most severe form of Hirschsprung disease by whole-genome sequencing. *Eur J Hum Genet.* 2018;26(6):818-26.
4. Li MX, et al. A comprehensive framework for prioritizing variants in exome sequencing studies of Mendelian diseases. *Nucleic Acids Res.* 2012;40(7):e53.
5. Xue Y, et al. Generating a non-integrating human induced pluripotent stem cell bank from urine-derived cells. *PLoS One.* 2013;8(8):e70573.
6. Gonzalez F, et al. An iCRISPR platform for rapid, multiplexable, and inducible genome editing in human pluripotent stem cells. *Cell Stem Cell.* 2014;15(2):215-26.
7. DeKelver RC, et al. Functional genomics, proteomics, and regulatory DNA analysis in isogenic settings using zinc finger nuclease-driven transgenesis into a safe harbor locus in the human genome. *Genome Res.* 2010;20(8):1133-42.
8. Lai FP, et al. Correction of Hirschsprung-Associated Mutations in Human Induced Pluripotent Stem Cells Via Clustered Regularly Interspaced Short Palindromic Repeats/Cas9, Restores Neural Crest Cell Function. *Gastroenterology.* 2017;153(1):139-53 e8.
9. Lau ST, et al. Activation of Hedgehog Signaling Promotes Development of Mouse and Human Enteric Neural Crest Cells, Based on Single-Cell Transcriptome Analyses. *Gastroenterology.* 2019;157(6):1556-71 e5.
10. Li P, et al. alphaE-catenin inhibits a Src-YAP1 oncogenic module that couples tyrosine kinases and the effector of Hippo signaling pathway. *Genes Dev.* 2016;30(7):798-811.
11. Lai FP, et al. Ciliary protein Kif7 regulates Gli and Ezh2 for initiating the neuronal differentiation of enteric neural crest cells during development. *Sci Adv.* 2021;7(42):eabf7472.
12. Liu JA, et al. Identification of GLI Mutations in Patients With Hirschsprung Disease That Disrupt Enteric Nervous System Development in Mice. *Gastroenterology.* 2015;149(7):1837-48 e5.
13. Hao Y, et al. Dictionary learning for integrative, multimodal and scalable single-cell analysis. *Nat Biotechnol.* 2024;42(2):293-304.
14. Morarach K, et al. Diversification of molecularly defined myenteric neuron classes revealed by single-cell RNA sequencing. *Nat Neurosci.* 2021;24(1):34-46.
15. Alayoubi Y, et al. Scanpro is a tool for robust proportion analysis of single-cell resolution data. *Sci Rep.* 2024;14(1):15581.
16. Bergen V, et al. Generalizing RNA velocity to transient cell states through dynamical modeling. *Nat Biotechnol.* 2020;38(12):1408-14.
17. Street K, et al. Slingshot: cell lineage and pseudotime inference for single-cell transcriptomics. *BMC Genomics.* 2018;19(1):477.
18. Qiu X, et al. Reversed graph embedding resolves complex single-cell trajectories. *Nat Methods.* 2017;14(10):979-82.
19. Yu G, et al. clusterProfiler: an R package for comparing biological themes among gene clusters. *OMICS.* 2012;16(5):284-7.
20. Aibar S, et al. SCENIC: single-cell regulatory network inference and clustering. *Nat Methods.* 2017;14(11):1083-6.

21. Ma Y, et al. Spatially informed cell-type deconvolution for spatial transcriptomics. *Nat Biotechnol.* 2022;40(9):1349-59.
22. Zhao L, et al. Mesenchymal-epithelial interaction regulates gastrointestinal tract development in mouse embryos. *Cell Rep.* 2022;40(2):111053.
23. Jin S, et al. Inference and analysis of cell-cell communication using CellChat. *Nat Commun.* 2021;12(1):1088.

Supplementary Table 1: List of oligos for gene targeting.

Genes/Allele	Orientation	Sequence (5' to 3')	Applications
hVCL full length	Forward	ATGCCAGTGTTTCATACGCGCACG	Generation of VCl expression vector
	Reverse	CTACTGGTACCAGGGAGTCTT	
hVCL-I20T	Forward	GGCACAGCAGaccTCCCACCTGG	Generation of Vcl-I20T
	Reverse	ACCGGCTCCAGGATGCTC	
hVCL-M209L	Forward	GTTGCTGCCAGTTCTCATTTCAGCTttgAAG ATTTTTGTAACAAC	Generation of Vcl-M209L
	Reverse	CCAGCTTCATCTAAGATCTG	
hVCL-A376G	Forward	CAAGCTGGAAggcATGACCAACT	Generation of VCL-A376G
	Reverse	CGAGCTGCATTTTCCACTTTTG	
hVCL-P398S	Forward	GCTTGCAGATtcaAATGGTGGAC	Generation of VCL-P398S
	Reverse	CAGTTCTGAGCAGCATCG	
hVCL-K666N	Forward	GGCCTCAGTGaatACGGCCCGAG	Generation of VCL-K666N
	Reverse	TGAATGCCTTCCACTGTTGATTTATTAGC	
hVCL-R1039Q	Forward	GGAGACTGTGcagGAAGCTGAAG	Generation of VCL-R1039Q
	Reverse	TTCACAGACTGCATGAGG	
hVCL-A977P	Forward	GCATCGGGAAcctACCAAGTGGTCTAGTAAGG	Generation of VCL-A977P
	Reverse	AAGGACTGAGCCGCGGCC	
hVCL Head Domain (aa1-258)	Forward	CTGGAATTCAATGCCAGTGTTTCATACGCG	Generation of Flag-Vcl head plasmid
	Reverse	CTGTCTAGACCAGGCATCTTCATCCCA AG	
hVCL Tail Domain (aa879-1066)	Forward	CTGGAATTCGGGAGGAAAAGGATGAAGAGTTC	Generation of Myc-Vcl tail plasmid
	Reverse	CTGCTCGAGACTACTGGTACCAGGGAGTC	
AAVS1 (1)	Forward	TTTCTTGGCTTTATATATCTTGTGGAAAGGACGAAACACCGTCACCAATCCTGTCCCTAG	Generation of iCas9-hiPSC line
	Reverse	GACTAGCCTTATTTTAACTTGCTATTTCTAGCTCTAAAACCTAGGGACAGGATTGGTGAC	
AAVS1 (2)	Forward	TTTCTTGGCTTTATATATCTTGTGGAAAGGACGAAACACCGCAGTGGGGCCACTAGGGAC	
	Reverse	GACTAGCCTTATTTTAACTTGCTATTTCTAGCTCTAAAACGTCCCTAGTGGCCCCACTGC	
VCL	Forward	CCACCTGGTGATAATGCACG	Generation of *VCL* KO ENCCs
	Reverse	GCTCGAGATTATCTAATTGA	

Remarks: mutated sequences are in small cap; the targeted sequences are underlined.

Supplementary Table 2: List of PCR primers for genotyping.

Genes/Allele	Orientation	Sequence (5' to 3')	Product size
Cre transgene	Forward	CGTACTGACGGTGGGAGAAT	374 bp
	Reverse	TGCATGATCTCCGGTATTGA	
Vcl$^{flox/flox}$	Forward	CATCATGAGTTCTTGACCTGGA	443 bp/550 bp
	Reverse	TGCAAACCCTAATAATTTTACGAA	
Ptn$^{-/-}$	Forward	CACACACACACACACACTATTGTTCACT	422bp/293bp
	Reverse	TGACACTGTAACAGTGTAACATTCTTGG	
	Forward	TCTAGGCATCTTTCATCTGGTAAAGGG	
	Reverse	CCCGGATGTCGCCTTATACAGTCA	
Rosa26^{YFP}	W-forward	CTGGCTTCTGAGGACCG	384 bp/184 bp
	W-reverse	CAGGACAACGCCCACACA	
	YFP-forward	AGGGCGAGGAGCTGTTCA	
	YFP-reverse	TGAAGTCGATGCCCTTCA	

Supplementary Table 3: List of primary antibodies used in this study

Primary antibody	Target antigen	Dilution	Assays	Category #	RRID
Mouse-anti-Tuj1	Neuronal classIII β-tubulin	1:500	IHC	Biolegend (801202)	AB_10063408
Rabbit-anti-Tuj1	Neuronal classIII β-tubulin	1:200	ICC	Abcam (ab18207)	AB_444319
Mouse-anti-HuD	ELAV Like RNA Binding Protein 4	1:200	IHC	Santa Cruze (SC-28299)	AB_627765
Rabbit-anti-nNOS	nNOS	1:100	IHC	Thermo Fisher Scientific (617000)	AB_2313734
Mouse-anti-Sox10 (CL4455)	SOX (SRY-related HMG-box) family transcription factors Sox10	1:100	ICC	Atlas Antibodies (AMAb91297)	AB_2665884
Goat-anti-Phox2b	Phox2b	1:100	IHC	R&D system AF4940	AB_10889846
Anti-alpha SMA	α-smooth muscle actin	1:500	IHC/ICC	Abcam ab21027	AB_1951138
Mouse-anti-Ki67 Clone B56	Human Ki67	1:100	IHC	BD Pharmingen 556003	AB_396287
Goat anti-Integrin beta 1/CD29	Recombinant mouse Integrin beta 1	10 µg/ml	IHC	R&D Systems AF2405	AB_416591
Rabbit anti-Vinculin	Vinculin	1:100	IHC	Abcam ab91459	AB_2050446
Mouse anti-Vinculin Clone hVIN-1	Vinculin	1:300	WB	Sigma-Aldrich V9131	AB_477629
Mouse anti-N-cadherin Monoclonal Antibody (3B9)	Cdh2, N-cadherin	1:100/1:1000	IHC/WB	Thermo Fisher Scientific 33-3900	AB_2313779
Rabbit anti-PTN antibody-C-terminal	Pleiotrophin	1:100	IHC	Thermo Fisher Scientific Cat# PA5-145351	AB_3094082
Rabbit anti-Cleaved caspase3	Activated caspase3 with cleavage adjacent to Asp175	1:100	IHC	Cell Signaling 9661	AB_2341188
Sheep anti-GFP	Green fluorescent protein and Yellow fluorescent protein	1:200	IHC	Bio-Rad 4745-1051	AB_619712
Chicken anti-GFP	Green fluorescent protein and Yellow fluorescent protein	1:200	IHC	Thermo Fisher Scientific A10262	AB_2534023
Rabbit anti-GFP antibody - ChIP Grade	GFP-tag	1:500	IP	Abcam ab 290	AB_303395
Chicken-anti-Neurofilament-Light (NF)	Neurofilament	1:200	ICC	Neuromics (CH22105)	AB_2737102
Rabbit-anti-PGP9.5	Protein gene product 9.5	1:200	ICC	Abcam (ab108986)	AB_10891773
Mouse anti-CRISPR-Cas9 Clone 7A9-3A3	Cas9	1:1000	WB	Abcam ab191468	AB_2692325

Rabbit anti-p44/42 MAP Kinase	p44/42 MAP Kinase	1:1000	WB	Cell Signaling Technology 9102	AB_330744
Mouse anti-Phospho-p44/42 MAPK	Phospho-p44/42 MAPK (Thr202/Tyr204)	1:1000	WB	Cell Signaling Technology 9106	AB_331768
Mouse anti-Actin, C4	Actin	1:20000	WB	Millipore MAB1501	AB_2223041
Mouse anti-FLAG M2	FLAG	1:10000	WB	Sigma-Aldrich F1804	AB_262044
Anti-FLAG M2 Magnetic Beads	Anti-FLAG M2 Magnetic Beads		IP	Sigma-Aldrich M8823	AB_2637089
Rabbit anti-c-Myc	c-Myc	1:1000	WB	ABclonal A19032	AB_2862524
Rabbit anti Myc-Tag pAb-C-terminal	Myc-Tag pAb-C-terminal	1:500	IP	ABclonal AE009	AB_2771925
Mouse anti-Paxillin, clone 5H11	Paxillin	1:2000	ICC/WB	Millipore 05-417	AB_309724
Rabbit-anti-Phospho-Paxillin (Tyr118) Polyclonal Antibody	Phospho-Paxillin (Tyr118)	1:1000	WB	Thermo Fisher Scientific PA5-143737	AB_2942965
CD271-FITC	Neurotrophin receptor $p75^{NTR}$	1:100	Flow cytometry	Miltenyi Biotec 130091917	AB_871651
HNK1-APC	CD57	1:100	Flow cytometry	BD Biosciences 560845	AB_10563760
ITGA4-PE	PE/Cyanine7 Anti-human CD49d	1:100	Flow cytometry	BioLegend 304314	AB_10643278

Supplementary Table 4. Secondary antibodies used in this study

Secondary antibody	Dilution	Applications	Category #	RRID
Donkey anti-Sheep IgG (H+L) Cross-Adsorbed Secondary Antibody, Alexa Fluor™ 488	1:500	IHC	Invitrogen A-11015	AB_2534082
Alexa Fluor® 488 Donkey Anti-Chicken IgG H&L	1:500	IHC	Jackson ImmunoResearch 703-545-155	AB_2340375
Donkey anti-Mouse IgG (H+L) Highly Cross-Adsorbed Secondary Antibody, Alexa Fluor™ 488	1:500	IHC	Invitrogen A-21202	AB_141607
Donkey anti-Rabbit IgG (H+L) Highly Cross-Adsorbed Secondary Antibody, Alexa Fluor™ 488	1:500	IHC	Invitrogen A-21206	AB_2535792
Donkey anti-Mouse IgG (H+L) Highly Cross-Adsorbed Secondary Antibody, Alexa Fluor™ 594	1:500	IHC	Invitrogen A-21203	AB_2535789
Donkey anti-Rabbit IgG (H+L) Highly Cross-Adsorbed Secondary Antibody, Alexa Fluor™ 594	1:500	IHC	Invitrogen A-21207	AB_141637
Donkey anti-Mouse IgG (H+L) Highly Cross-Adsorbed Secondary Antibody, Alexa Fluor™ 647	1:500	IHC	Invitrogen A-31571	AB_162542
Donkey anti-Rabbit IgG (H+L) Highly Cross-Adsorbed Secondary Antibody, Alexa Fluor™ 647	1:500	IHC	Invitrogen A-31573	AB_2536183
Donkey anti-Goat IgG (H+L) Cross-Adsorbed Secondary Antibody, Alexa Fluor™ 647	1:500	IHC	Invitrogen A-21447	AB_2535864
Goat-anti-rabbit HRP	1:2000	WB	Dako Cytomation (P0448)	AB_2617138
Goat-anti-mouse HRP	1:2000	WB	Dako Cytomation (P0447)	AB_2617137